

Review

Design Methodology and Application of Surface Texture: A Review

Ange Nsilani Kouediatouka^{1,2} , Qiang Ma^{1,2}, Qi Liu^{1,2}, Fagla Jules Mawignon^{1,2}, Faisal Rafique^{2,3} 
and Guangneng Dong^{1,2,*}

- ¹ Key Laboratory of Education Ministry for Modern Design and Rotor Bearing Systems, Xi'an Jiaotong University, Xi'an 710049, China; angensilani@stu.xjtu.edu.cn (A.N.K.); maqiang@nwpu.edu.cn (Q.M.); liuqi1029156055@stu.xjtu.edu.cn (Q.L.); mawignon@stu.xjtu.edu.cn (F.J.M.)
- ² Department of Mechanical Engineering, Xi'an Jiaotong University, Xi'an 710049, China; engr_faisalrafique@hotmail.com
- ³ State Key Laboratory for Strength and Vibration of Mechanical Structures, School of Mechanical Engineering, Xi'an Jiaotong University, Xi'an 710049, China
- * Correspondence: donggn@mail.xjtu.edu.cn

Abstract: Surface texture is regarded as a promising solution for enhancing the tribological features of industrial materials due to its outstanding benefits, such as minimization of the contact area, enhancement of the load bearing capacity, storage of the lubricant, and management of the transition between lubrication regimes. Surface texture can be processed under either liquid or gas conditions. As compared to laser ablation in air, employing liquids or other gases as ablation media provides high accuracy and uniformity by limiting the heat-affected zone (HAZ) and other undesired defects to a large extent, as well as high crater structural features. In addition, the synergistic use of different liquid, solid, and additive lubricants with surface roughness recently demonstrated excellent performance. Therefore, surface texture helps to improve the tribological characteristics of a material. This paper reviews the design methodologies and applications of surface texture, emphasizing the proper selection of the appropriate laser parameters and ambient conditions for the best texture quality and functionality. Recent texture geometric design features to improve the film thickness and the self-lubricating system are presented. The ablation environment is explored using various media. The interaction between the lubricants' types and surface textures is explored based on the operating conditions. Furthermore, surface texture applications using superhydrophobic surfaces, anti-drag, and vibration and noise friction are discussed. We hope that this review plays an enlightening role in follow-up research on laser surface texture.

Keywords: laser surface texturing; design methodology; processing medium; lubrication; anti-drag; vibration and noise



Citation: Nsilani Kouediatouka, A.; Ma, Q.; Liu, Q.; Mawignon, F.J.; Rafique, F.; Dong, G. Design Methodology and Application of Surface Texture: A Review. *Coatings* **2022**, *12*, 1015. <https://doi.org/10.3390/coatings12071015>

Academic Editor: Anatoly Kovalev

Received: 1 June 2022

Accepted: 9 July 2022

Published: 18 July 2022

Publisher's Note: MDPI stays neutral with regard to jurisdictional claims in published maps and institutional affiliations.



Copyright: © 2022 by the authors. Licensee MDPI, Basel, Switzerland. This article is an open access article distributed under the terms and conditions of the Creative Commons Attribution (CC BY) license (<https://creativecommons.org/licenses/by/4.0/>).

1. Introduction

One of the current objectives in engineering applications is undoubtedly a reduction in friction and wear for the prolongation of industrial equipment's lifespan. In fact, every surface has some kind of texture, defined by profile, volume, and areal parameters and responsible for fatigue crack and fractures on surfaces, which result in functionality loss. However, depending on the application area and region, some of these parameters are considered vital to surface functionality. A limited number of parameters is recommended to avoid the "parameter rash" [1,2]. Based on the effect of the surface morphology on the behavior of surfaces, surface texturing, which is a method that creates micro-pits, such as dimples [3] and grooves [4], on the mating surface under dry and lubricated conditions [5], was developed to lower friction and wear. From the work of Etsion's group [6] surface texturing modeling and design gained great interest with their potential for improving tribological behavior.

Texturing methods can be broadly classified into four categories: addition, removal, displacement of material, and self-forming methods [7], with a large number of surface texturing technologies, including: mechanical methods [8], etching technologies [9], coatings [10], and laser-based techniques [11]. Laser-based methods have numerous advantages over the other three methods, such as an absence of tools' contact with the surface, operation simplicity, a friendly environment, and the capacity to produce a variety of pits in a wide range of material. The laser-based methods include laser shock processing [12], Laser ablation [13], and Laser interference [14]. Among these three laser-based methods, laser ablation, commonly called LST (laser surface texturing), is the most flexible and is subjected to a much easier procedure [15]. Laser ablation has developed from long-pulse or nanosecond (ns) lasers, which created large heat-affected zones (HAZ), oxide amounts, and defects to short and ultra-short pulse lasers known today as femtosecond (fs) and picosecond (ps) lasers, respectively; these short and ultra-short pulse lasers improve the ablation quality with fewer drawbacks. Cernasejus et al. [16] employed a nanosecond laser to modify surfaces in an oxidizing environment. A large amount of oxides was produced during the processing procedure, which decreased the surface quality. Trucchi et al. [17] employed an ultra-short laser for diamond micro-structuring because of the reduced thermal effects, as well as an effective surface nano-structuring. Ultra-short pulse lasers have been the most popular way to circumvent long-pulse lasers' limitations. However, during the laser process, burrs and heat are generated, which may be controlled using a processing medium [18,19].

Various texture parameters have been applied to mechanical components to improve their tribological performance, including: shape, size, area density, area ratio, and working conditions. Relevant researchers investigated the mechanism of improvement in the friction and wear of concave and convex textures [20–25]. Five main mechanisms were revealed: the surface hardness [23], the wear debris particle storage [25], the reduction in the real contact area [24], the lubricant reservoirs [26], and the micro-hydrodynamic pressure [27]. In the past few years, extensive theoretical and numerical investigations have been conducted, and significant progress has been achieved regarding surface texture technology. Gropper et al. investigated the geometric features of surface texture and found that the shape, texture ratio, area density, dimple orientation, and position are crucial for an efficient and good texture design [28]. In addition, Hu et al. looked at the influence of four cross-grooved texture shapes on the tribological performance. Under a high sliding frequency and low load, the hexagonal shape texture outperformed the other three in terms of friction, contact stress reduction, and oil film generation [29]. Sun et al. investigated the friction and wear properties of dents' texture rolling element bearings under dry wear. According to the findings, a combination of textural parameters, such as diameter, depth, and orientation, can reduce the wear rate [30]. In addition, Profito et al. [31] showed that the operating lubrication regime was the main factor for friction reduction. On the other hand, Ma et al. [32] combined surface texture, thermal oxidation, and a Polytetrafluoroethylene (PTFE)-based lubricant coating. The results revealed that PTFE boosted with thermal spraying on the surface texture improved the tribological performance. Furthermore, Grützmacher et al. [33] experimentally examined the influence of single and multilayer textures on the friction reduction. There was a change in the switch from a mixed lubrication regime to a hydrodynamic one. Later, Grützmacher et al. [34] discovered that the multilayer texture had a lot of potential for guiding lubricant around the surface.

The purpose of this paper is to present advancements in the effects of laser ablation; the solution used to deal with unwanted phenomena that slow down the machining process, such as the generation of burrs; the non-uniform crater morphology; and the thermal effect of the laser beam by manipulating the laser parameters and introducing processing media, as framed in Figure 1. We present the process design of the surface texture, with the latest texture shape acting as a self-lubricating system; effects of the working parameters, such as load and sliding frequency, on lubrication; and the introduction of potential lubricants to deal with traditional lubricants' limitations. In addition, we present surface

texture applications, including super hydrophobicity, anti-drag, and vibration and noise for mechanical equipment, followed by the conclusion and outcomes.

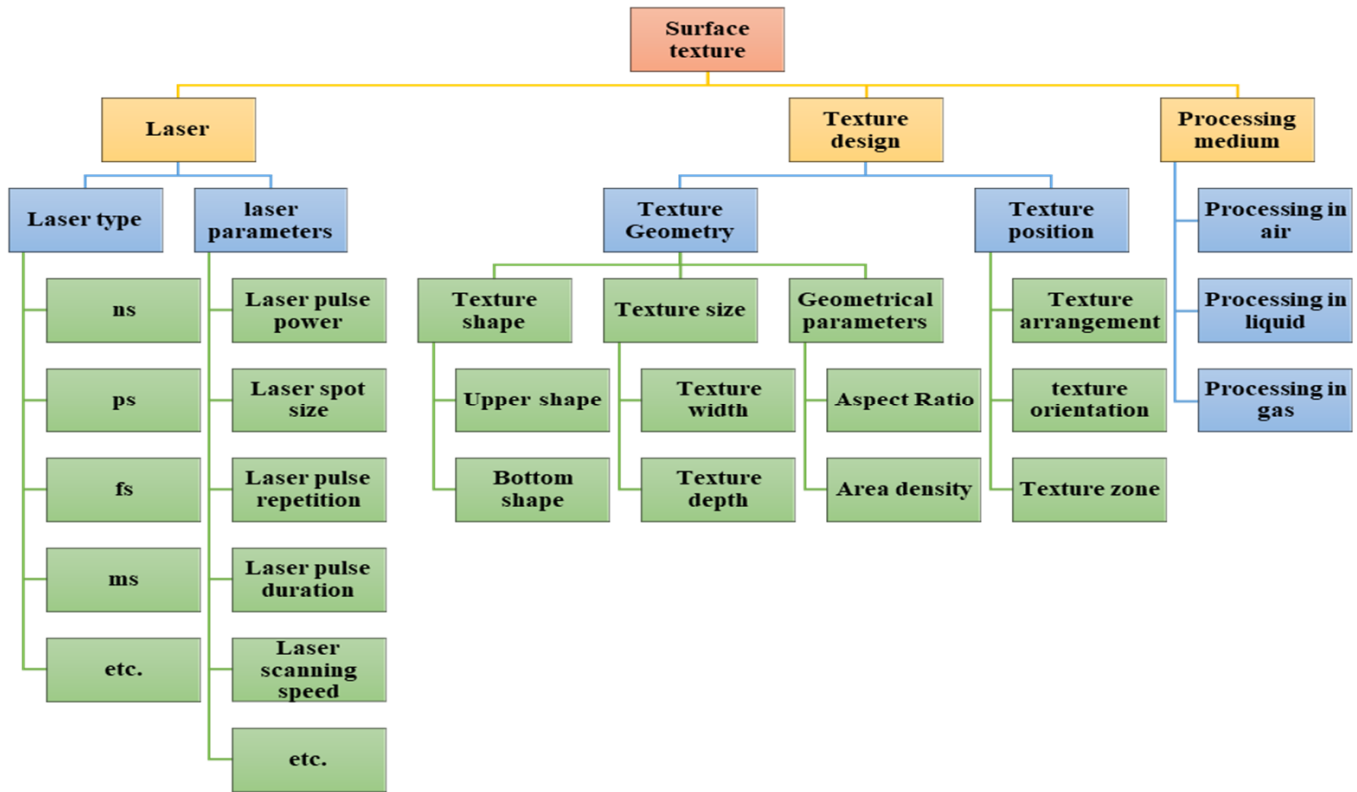


Figure 1. Laser surface texture technology features.

2. Effect of Laser Pulse Properties

Laser surface texturing essentially includes nanosecond, picosecond, and femtosecond lasers. Although these various types of lasers can perform patterns, the desired pattern morphology requires a methodic manipulation of various laser parameters. However, only a few parameters, including the laser type, laser power intensity, laser scanning speed, and pulse repetition, will be reviewed. In addition, the choice of ambient conditions and the nature of the target material are as crucial as the laser parameters [35,36]. Table 1 shows an examination of the effect of the laser parameters on the substrate material.

Table 1. Analysis of different types of lasers with respect to the laser parameters and nature of the material.

Material	Type of Laser	Laser Pulse Power (w)	Laser Pulse Repetition Rate (kHz)	Laser Scanning Speed (mm/s)	Micro Hardness (HV)	Depth (μm)	Width (μm)	Findings	Ref
50CrMo4 steel	Millisecond laser	27	0.01	2	700 HV	200	—	A depth of 1000 μm can be achieved with ms laser parameters.	[18]
	Nanosecond laser	90	500	200	642 HV	80	—		
Tin Bronze	Femtosecond laser	0.1	—	5–10	—	1.256–2.94	12.21–14.21	Lower scanning speed, led to deeper and wider grooves.	[37]
20CrNiMo beryllium bronze	Femtosecond laser	5×10^{22} – 25×10^{22}	100	—	—	28.007–33.983	169.266–70.398	Laser peak power and exposure duration produced the optimal crater size.	[38]
5A06 aluminum alloy	Nanosecond laser	15×10^5	50	41.66	355.08	—	—	For the nanosecond laser, the HAZ was clearly visible.	[39]
Silicon Nitride	Nanosecond laser	50	100	2–100	—	—	—	At a low pulse intensity, the laser cuts created by the ps laser had smoother surfaces and straighter edges than the ns laser with a decreased HAZ and thermal damages.	[40]
	Picosecond laser	50	100	2–100	—	—	—		
Leaded brass	Femtosecond laser	5–15	100–300	5–15	168–189	100–200	10–25	The improved surface roughness and the hardness of the material decreased the friction; wear increased in dry conditions.	[41]

—: Not reported.

2.1. Laser Type

Various laser pulses are used in LST to focus a laser beam on the surface of a material, as shown in Figure 2. During the process, the electrons absorb energy regardless of the pulse duration, increasing the kinetic energy of the system. However, the amount of energy transferred to the bulk is highly dependent on the pulse duration [42–44]. Long pulses (Figure 2a) through thermalization lead to the formation of surface debris, microcracks, and a high heat-affected zone, which change the surface chemistry and structure [45], thus resulting in a continuous melting and re-solidification process. In Figure 2b, short pulse durations consist of a combination of moderate melting and solidification, straight evaporation, and, thus, a small HAZ [42]. Ultra-short pulses limit the formation of heat and the laser–material interaction to direct evaporation due to the short period of energy deposition (Figure 2c) [41].

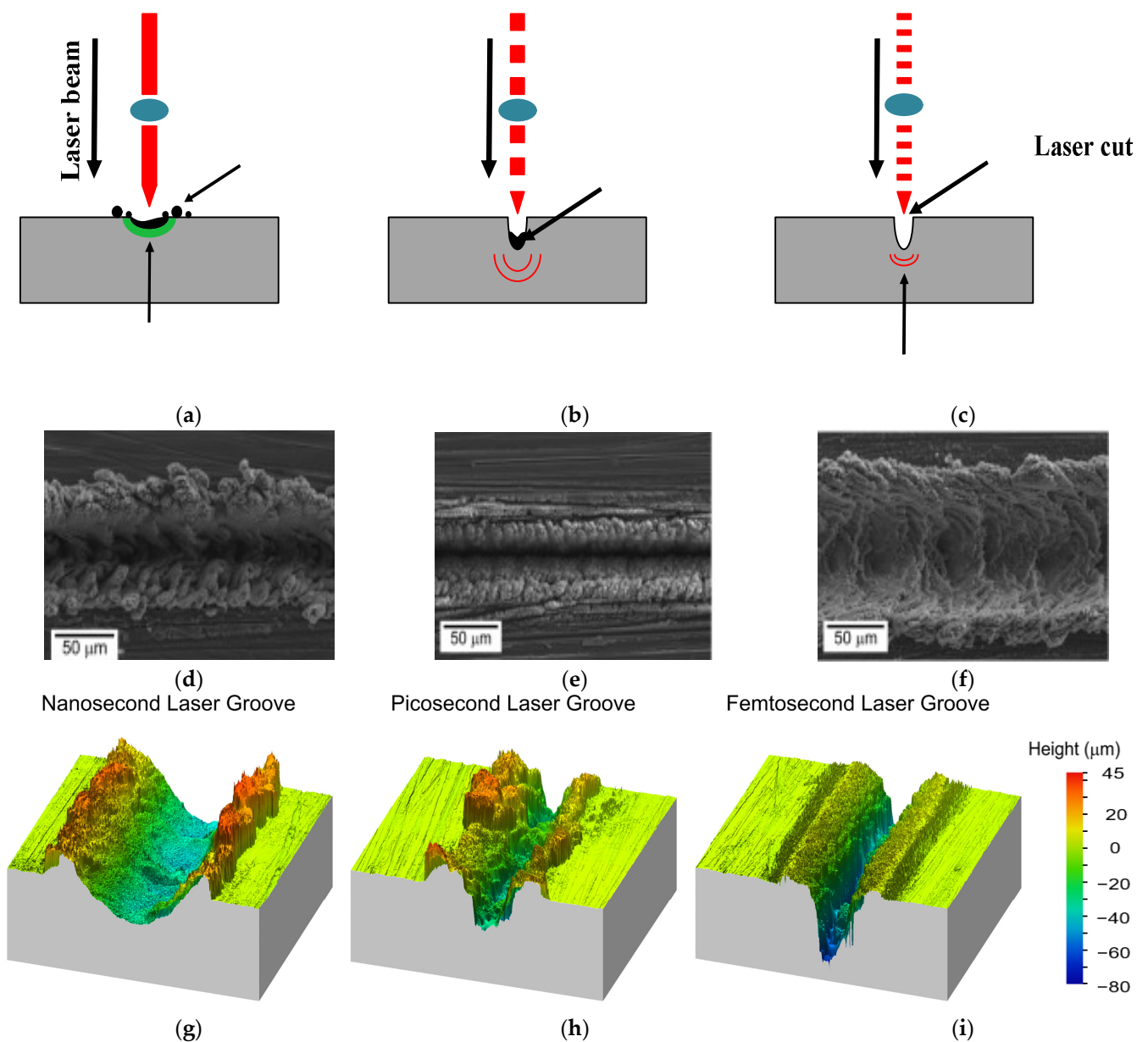


Figure 2. Classification of lasers based on pulse durations: (a) long pulse, (b) short pulse, and (c) ultra-short pulse; SEM images of surface morphology with: (d) ns laser, (e) ps laser, and (f) fs laser; surface texture cross-section profiles generated with: (g) ns laser, (h) ps laser, and (i) fs laser, Reprinted with permission from [46]. Copyright from Elsevier 2021.

Ultra-short and short laser pulse techniques can lead to controlled ablation and a micro-texture with a moderate heat-affected zone, as well as fewer burrs and defects compared to long pulse lasers [46]. As illustrated in Figure 2d,e, the surface texture created with short and ultra-short pulse lasers exhibits plateau-like surface patterns with fewer bulges or rims than those made with long pulses (Figure 2f). In addition, differences in the depths ($fs > ns > ps$) and widths ($ns > fs > ps$) can be noticed in Figure 2g–i. A short laser pulse ablation is melt-free with a minimal thermal impact, no visible material pile-up, and no convex shape on the ablation edge [41,42]. As a result, femtosecond pulses have more advantageous effects on the HAZ compared to nanosecond, picosecond, and millisecond pulses [37,38].

Nanosecond laser ablation was more effective for smooth ablation compared to femtosecond, picosecond, and millisecond laser ablation [18,45,47]. This could be due to the superior hardening effect of the nanosecond laser compared to femtosecond and picosecond lasers, which can result in direct ablation and the removal of material (Figure 2a). Nanosecond laser methods are cheaper and more efficient than picosecond and femtosecond lasers and have great potential in large-scale industrial applications [48,49]. Unfortunately, the drawbacks associated with the high-energy photons in nanosecond lasers result in an expanded heat-affected zone with multiple defects and the production of bulges [45] (Figure 2g), which lowers the surface quality significantly compared to picosecond (Figure 2h) and femtosecond lasers (Figure 2i) [40]. The pulse duration has a significant impact on the laser–material interaction. Selection is based on the cost, the required geometry, the substrate material, and the application. However, the effect of the laser type on the surface can be controlled by adding a processing medium to reduce the thermal damage and bulges on the material’s surface [19].

2.2. Laser Power Intensity and Scanning Speed

The machining process, the size of the crater, and the hardness of a material can be enhanced by adjusting and controlling the laser power intensity with a direct effect on tribological performances [38,39,50–53]. Liu et al. [51] used a laser power density of 0.32 GW/cm^2 on TC4, the treated surface that had the lowest COF and wear rate. During laser processing, the fractures that separated cells in the cell-like surface texture had regular edges. In another study, by changing the peak power and irradiation time, various geometric characteristics were obtained, and the friction was reduced by more than 52% [38]. Laser powers with various pulse numbers can further enhance the inner and outer sizes of the crater and contain wear debris, thereby keeping the surface clean. In Figure 3a, the area of the crater increases with the increase in the laser fluence and number of pulses.

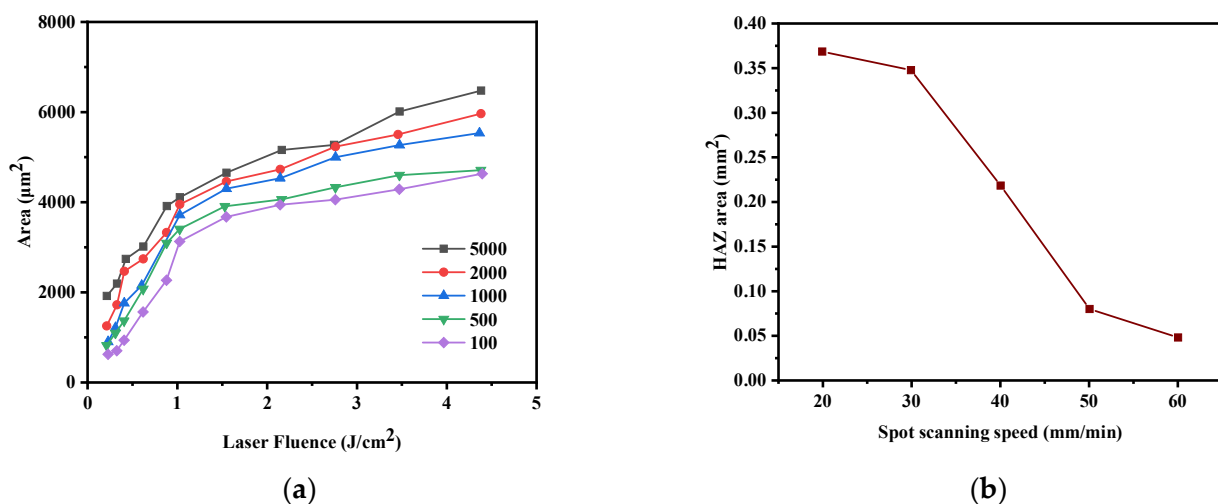


Figure 3. Cont.

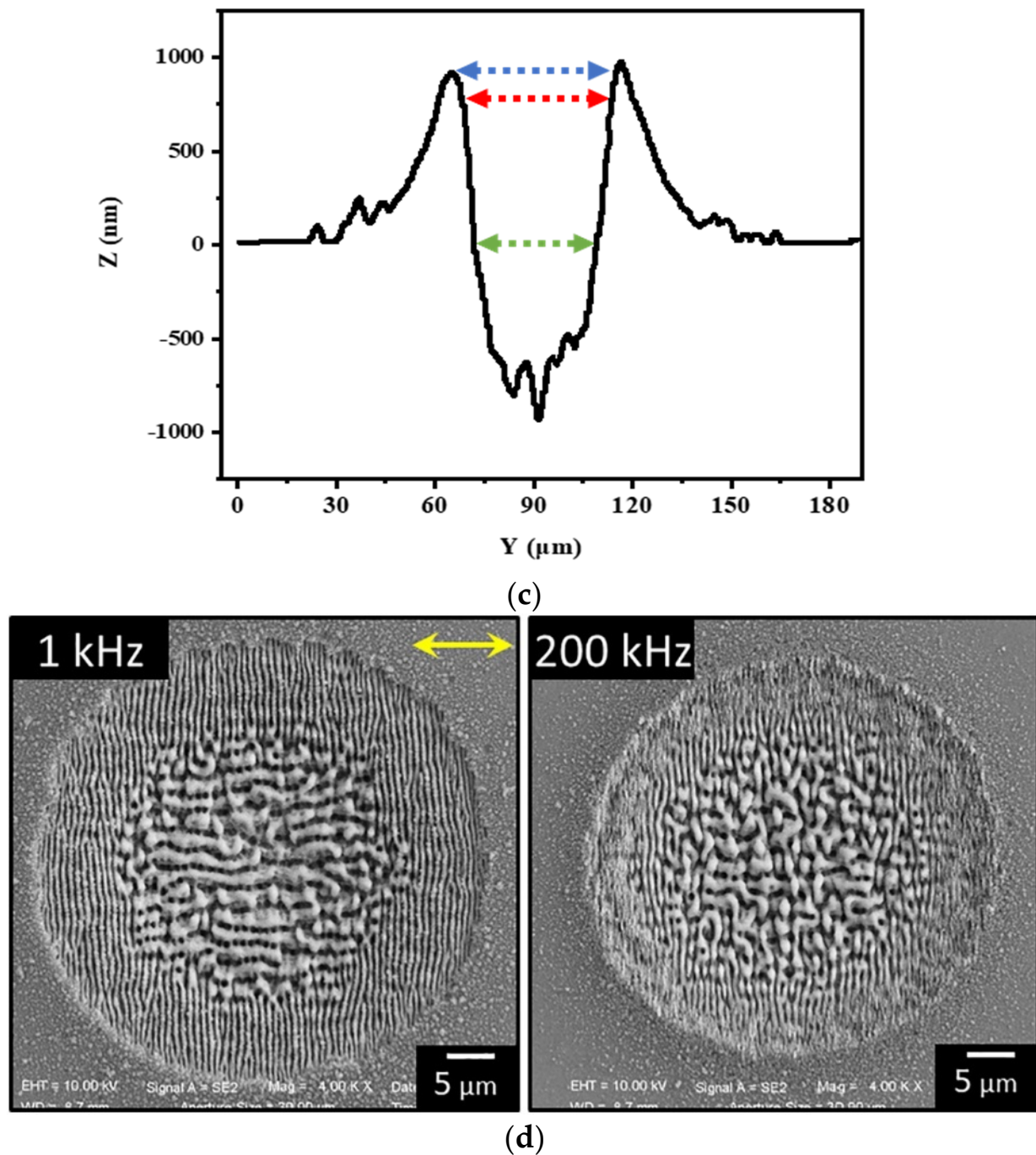


Figure 3. (a) Area of the drilled crater with different laser fluences ranging from 100 to 5000, reprinted with permission from [50], copyright from Elsevier 2019; (b) impact of laser scanning speed on the heat-affected zone, reprinted with permission from [54], copyright from Elsevier 2017; (c) cross-section profile of a crater along a horizontal dashed line, reprinted with permission from [52], copyright from Elsevier 2020; (d) SEM images of the irradiated silicone sample with $N = 200$ pulses at an energy $E = 7 \mu\text{J}$, in air, for two different pulse Repetition rate: (left) 1 kHz; (right) 200 kHz. The yellow arrow in the left panel shows the direction of the laser beam polarization, reprinted with permission from [55]. Copyright from Elsevier 2019.

Scanning speed is another critical laser parameter for producing textures with irregularities and can regulate the material removal and the depth [37]. Jia et al. [39] conducted a study on the impact of the processing parameters on the hardness of textured 5A06 aluminum alloy. It was discovered that a low value of the scanning speed was most beneficial for improving the hardness, followed by the pulse frequency. In addition, Salgero et al. [53] produced various texture types of titanium Ti6Al4V by changing the energy density and the scanning speed. Although both factors were shown to be advantageous, the scanning speed outperformed the energy density, reducing the friction and wear volume by approximately 62% and 80%, respectively. Scanning speed was proven to improve the roughness, the crater morphology, the HAZ, and the tribological performance at lower speeds [37,41,54]. In Figure 3b, the HAZ is shown to decrease dramatically as the laser spot scanning speed increased. This is due to the reduction in the total heat energy and the energy at the bottom of the pits. During the machining process, a relatively low scanning speed should be employed in order to generate a hole with a comparatively small HAZ region, since higher scanning speeds have a lower pulse overlap effect, which results in a lower material removal rate.

2.3. Pulse Repetition Rate

Pulse repetition (high or low) has an impact on the material removal rate and the generated crater morphology in laser ablation [47,52,55,56]. Allahyari et al. [52] investigated the influence of the pulse repetition rate on the pit features in the range of 10 Hz to 200 Hz with the fixed number of pulses at 100. The result showed that a high repetition rate led to a reduction in the crater size and volume, with an increased crater volume (Figure 3c) [52]. An intriguing morphological divergence in the SEM images is shown in Figure 3d. In fact, the crater formed at 200 kHz (right) is 25% smaller than the one formed at 1 kHz (left), and nanoparticle debris can be seen covering the outer area near the shallow crater in both of the following situations: the formation of supra-wavelength grooves in the central zone of the relatively shallow groove for 1 kHz, and the formation of a channel of micro-sized, spherically shaped, crochet-like structures in the central part of the hole for 200 kHz. These nanoparticles are produced during the material degradation that occurs after the laser ablation of the silicon substrate and the redeposition the material due to the high-pressure, atmospheric ambient gas [55].

3. Effect of Geometric Characteristics of Textured Surfaces

The coefficient of friction (COF) is strongly influenced by the geometric characteristics of surface texture, including: shape, size, area ratio, area density, orientation, arrangement, and sliding direction. Some research works have carried out the geometric characteristics shown in Table 2. In Section 3, we discuss the standard geometric parameters, as well as the newest texture design, for a reduction in friction and wear.

Table 2. Influence of various geometric characteristics on tribological properties.

Ref	Geometric Characteristics					Observation
[57]	shape	Diameter (μm)	Depth (μm)	Area ratio	Area density	The dimple contour profile appears to have an influence on the area density (35%), as does the depth on the area ratio; the ellipsoidal shape provided the highest LCC.
	spherical	—	—	0.0070	15%	
	ellipsoidal	—	—	0.0036, 0.0081	35%	
	circular	—	—	0.0035	15%	
	elliptical	—	—	0.0017, 0.0038	35%	
	triangular	—	—	0.0035	10%	
chevron	—	—	0.0035	10%		
[58]	circular	40–90	9.6	—	26%	The rectangular texture was discovered to have the highest LCC of all the patterns.
	rectangular	40–90	7.2	—	17%	
	square	40–90	7.2	—	20%	
	Triangular	40–90	9.6	—	21%	
[59]	Crosshatch groove texture	5	10–100	0.0–5–0.125	20%	The crosshatch angle and area ratio of the pattern appeared to be crucial to obtaining the lowest COF
[60]	Overlap droplet + parallelogram	9.5, 45	2.08, 0.90	—	5%–17.5%	Both mixture and overlaps had an impact on the friction coefficient with up to an 80% reduction. The overlap with the 5% area density outperformed that of the 7% and the mixture.
	Mixture droplet + parallelogram	12.8, 45	2.26, 0.90	—	5%–17.5%	
[61]	circular	—	7.5–10	—	4%–9.5%	Elliptical dimples reduced friction by up to 20%, followed by circles, rectangles, and diamonds. With a 0° orientation angle, the optimal area density was chosen as 4%.
	elliptical	—	7.5–10	—	4%–9.5%	
	diamond	—	7.5–10	—	4%–9.5%	
	rectangular	—	7.5–10	—	4%–9.5%	
[62]	Linear groove	100	7–19	0.07, 0.19	10%	Grooves oriented between 0° and 90° to the sliding direction reduced friction by 44%. Grooves of 7-depth worked better at low pressure, reducing friction by 38.2%, while 19-depth grooves performed better at high pressure.
[63]	Spherical	900	60	—	7.5%–20%	The lubrication regime was influenced positively by the dimple shapes with an area density of less than 20%. The long drop and the spherical oil pocket outperformed the short drop.
	Long drop spherical	500	55	—	7.5%–20%	
	Short drop spherical	800	60	—	10%–20%	

Table 2. Cont.

Ref	Geometric Characteristics				Observation
[64]	Circular + elliptical	300	6.5	—	Multi-shape patterns with an area density of less than 20% reduced the COF under prolonged sliding situations, thereby maintaining the surface quality.
	Circular + square	500, 250	6.5	—	
	Circular + triangular	500, 250	6.5	—	
[65]	Grid groove	—	—	—	The COFs of the grid, asterisk, and circle's groove patterns decreased by 10.55%, 6.03%, and 9.50%, respectively, while their wear rates increased by 47.05%, 41.48%, and 27.21%, respectively, when compared to the smooth surface.
	Circle groove	—	—	—	
	Asterix groove	—	—	—	

—: Not reported.

3.1. Effect of the Texture Shape

Texture pit is characterized by an upper shape and a bottom shape. The upper shape can have various morphologies, including concave (Figure 4a) and convex textures [58,61,66,67] (Figure 4b). Hemisphere dimples and grooves are the first standard concave and convex texture pattern ever created.

Many studies have been conducted regarding the standard design used in surface texture technology, with relatively great tribological performances [29,57,61,63,65]. According to Boidi et al. [3], a hemisphere dimple can reduce friction by up to 20% and promote hydrodynamic lubrication at a specific low speed, whereas grooves exhibited little advantageous or negative effect on the COF [67]. However, in another study, the groove texture's tribological properties outperformed round and other shapes [41]. The geometry, the operating conditions, and the application of these two types of texture, as well as the lubrication regime, may all contribute to this difference. For face milling applications [67], fluid from the end of the groove that reaches the tool–chip contact area can lead to higher lubricity than in closed shapes, but the groove's open geometry does not keep the lubricant in a circular shape, which is excellent for lubricant storage under solid cutting conditions. The circular shape performs better than grooves in compressive lubricants. Nevertheless, the size of concave textures might cause them to lose their effectiveness.

Some scientists have developed non-standard shapes, as illustrated in Figure 4c, to counter the standard texture limitations. Many numerical studies [28,68–71] were conducted focusing on the SQP (sequential quadratic programming) algorithm. When comparing the convex textures of grooved designs' shapes, such as herringbone, sinusoidal, and taper-flat, the taper-flat shape provided a better pressure distribution, load bearing capacity (LCC), and radial stiffness than other patterns [28]. In addition, Maldonado-Cortes et al. [67] found that the "S" groove's geometry exceeds the overall performances over the other shapes. Furthermore, by varying the crosshatch angle and size, the grooved crosshatched designs were able to reach considerable friction improvements [59]. In addition, the GA-SQP (genetic algorithm–sequential quadratic programming) method has been used for the optimization of V shape, thereby improving the LCC and leakage with an ultra-low COF under specific situations [68–71]. Similarly, for a concave texture, using a genetic algorithm (GA), Zhang et al. [66] created a bullet and fish-like texture pattern for unidirectional movement. The bullet and fish forms were found to have lower friction coefficients than circular dimples, both numerically and experimentally. However, the optimized shape has no advantage over a round pit texture under low speed and severe load. From the aforementioned literature, it can clearly be seen that irregular shapes have a greater effect on tribological performances than standard concave and convex textures.

Nevertheless, to ensure the lubricant supply at the interface and the wear debris storage, the internal structure of the texture is of the utmost importance. A flat bottom is commonly used in surface texture, and its ability to lower the friction coefficient at high speeds or under heavy loads has been demonstrated. However, flat bottom profiles, such as wedge-shapes, can enhance the load-carrying capacity and, thus, increase the friction performance [69]. Shen et al. [72] looked at the effect of the internal structure of dimples on hydrodynamic lubrication by comparing three bottom shapes, including: rectangular, oblique triangular, and isosceles triangular. Their findings demonstrated that cylindrical dimples with a rectangular cross-sectional form had a significant impact on the LCC. The ability of the internal structure for lubricant storage and release might be the reason for these positive benefits. However, under some working conditions, such as Hertzian contact, starvation of the mating surface, or an inadequate lubricant supply on the interface, result in high friction [73].

Combining a variety of texture types is essential for enhancing the lubrication properties; since different textures have distinct effects, a combination will further enhance the tribological behavior [60,64]. A multi-layer textured surface might improve the lubricant storage and effectively capture wear debris. Combinations, such as rectangular–spherical and rectangular–rectangular dimples [69] or circular dimples–ellipses [74], were demon-

strated to speed up transitions between lubrication regimes as well as enhance the LCC and the COF, as compared to a single texture type. Mixing concave and convex textures might be a way to give the resulted texture additional features. Segu et al. [75] recently developed a combined texture made by a circular dimple and a wavy groove, resulting in an improved friction coefficient. These beneficial effects might be explained by the largest combined converging wedge and the smallest separation, which were triggered by different texture shapes and act as oil reservoirs. However, the texture size is crucial to maximizing the effect of a compound pattern, since a deep pattern can store lubricant efficiently, while a wide design can trap debris, leading to a longer oil lifetime [76].

Numerous new texture surface designs with better tribological performances than traditional textures were proposed with a self-lubricant supply system on the contacting surface. By using a biomimetic approach, Zhao et al. [77] produced a self-replenishing lubricating system inspired by earthworms for adaptive friction-reduction and antifouling surfaces. The system was able to secrete oil on the surface layer when pressure was applied, and, after unloading, the droplets and boundary were restored. The friction coefficient and wear resistance were both significantly reduced by the design. In addition, Wang et al. [78] reported a novel texture design with pockets for improving the tribological properties of point contact under starved lubrication to deal with the lubricant supply and the surface contact stress (Figure 4d). The design worked as a lubricant storage (Figure 4e) and release system (Figure 4f), as well as a surface contact pressure homogenizer. The textured sample ensured a COF reduction of approximately 40%. It may be deduced from the discussion above that the influence of surface texture shape on the tribological performance is not dependent on a single parameter.

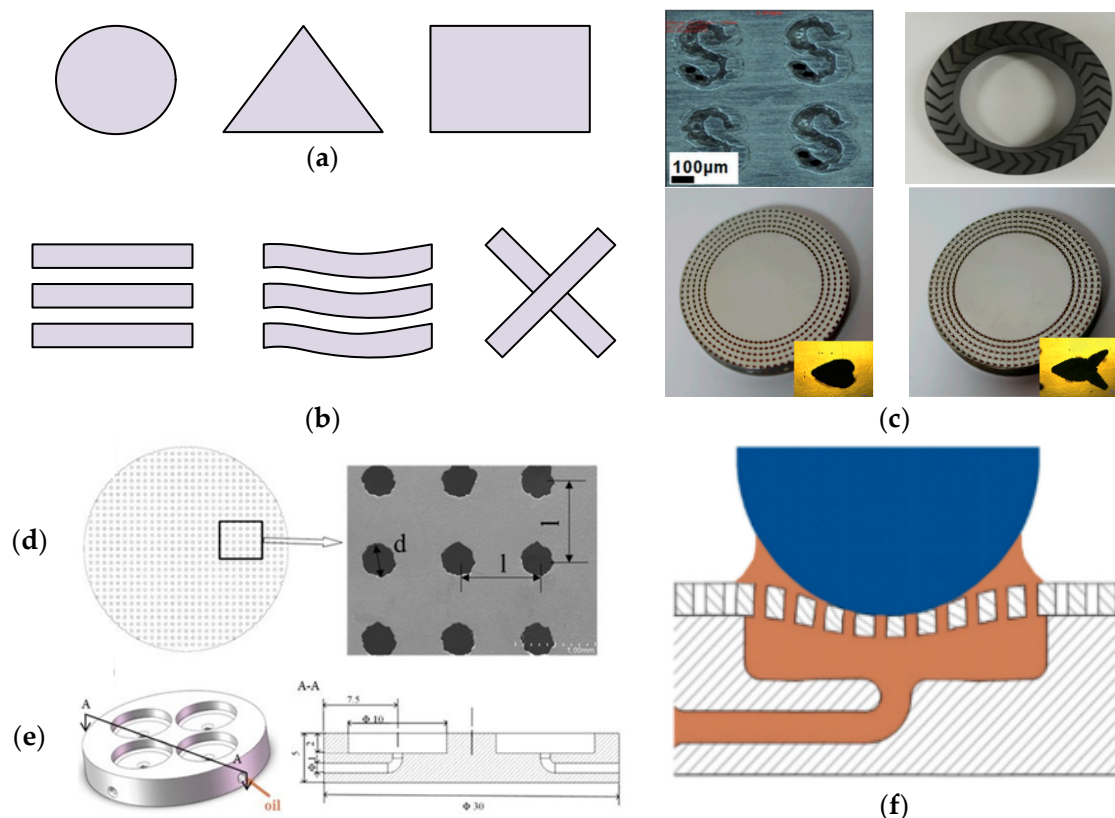


Figure 4. Texture shapes: (a) concave textures; (b) convex textures; (c) optimized texture shapes—“S” groove, “V” shape—reprinted with permission from [67,71], copyright from Elsevier 2021, 2015; bullet and fish shapes—reprinted with permission from [70], copyright from Elsevier 2017 (d) textured surface illustration; (e) pocket substrate model; (f) pocket—textured surface sample’s effect under applied load, reproduced with permission from [78].

3.2. Effect of the Texture Size

The texture size (depth and diameter) has a considerable effect on the tribological properties by storing the lubricants, trapping wear debris, avoiding the oil layer rupture, and enhancing the load bearing capacity [75]. The impact of groove size on the enhancement of tribological properties under sand–oil lubrication was explored by Dongya et al. [66]. It was discovered that the width could contain wear debris in the hole, thereby preventing sand migration on the sliding contact and lowering friction and wear. Nevertheless, the wear increases with the pattern size. In general, increasing a dimple's diameter means more hydrodynamic effect to reduce contact between the mating surfaces. However, when the diameter is larger than the contact width, the interference of a nearby pressure peak and the pressure trough of two adjoining textures may reduce the hydrodynamic effect. Nevertheless, oil is trapped as the depth increases, and the lubrication mechanism can shift from boundary to starved lubrication leading to higher friction and wear [41,61]. In that view, shallow and small circularly patterned dimples had a more noticeable effect on the hydrodynamic pressure, thus the friction reduction. The performance of dimple size also depends on the lubrication regime. In boundary lubrication, the highest friction reduction effect is generated for all of the dimpled surfaces, potentially due to the secondary lubrication. In EHL (electrohydrodynamic lubrication) contact, shallow dimples resulted in enhanced film thickness, but deep dimples resulted in film collapse [62]. When the optimum tribological performance is required, the influence of depth is preferable to the diameter [73]. However, the surface texture is gradually removed with wear, when the depth is small, which may cause the friction to increase again [74].

3.3. Effect of Area Density and Area Ratio

Many studies [61,67,74,79–82] have investigated the influence of the texture–area ratio and area density with the optimal choice ranging from 5% to 20% for the area density and smaller than 1 for the area ratio to enhance the LCC and friction coefficient. Ding et al. [61] found that an area density of 4% is advantageous for friction reduction on cast iron. Additionally, some previous research found a 16% area density to be optimum for lowering the COF and wear [67]. On the other hand, a dimple area ratio of 0.1 μm and a dimple area density of 20% reduced the friction by 40% [74]. The load bearing capability of the surface texture decreases as the area density rises, lowering the tribological features [61]. Recently, four different densities of 10%, 15%, 20%, and 25% with corresponding aspect ratios of 0.16 and 10% (texture 1), 0.16 and 15% (texture 2), 0.16 and 20% (texture 3), 0.16 and 25% (texture 4), and 0.08 and 10% (texture 5) were investigated [75]. The reference sample T6 and the simple texture samples T7 (circles/dimples) and T8 (sine wave channels) were also tested and compared. The best tribological performance was performed by texture 1 for a 10%–15% area density and a 0.16 area ratio.

3.4. Effect of Texture Arrangement, Orientation, and Sliding Direction

The texture is arranged and distributed on the surface in a multitude of ways. The most common texture arrangements used in current research are square, staggered, and radiating lattices. The texture arrangements had a substantial impact on the LCC, hydrodynamic pressure, and many other properties [62–82]. Hua et al. [83] arranged square and staggered patterns on the surface of a DF2 utility knife. The staggered texture had a better lubricating effect. In addition, Zhang et al. [25] compared two texture arrangements: the square and the linear radiating arrays. The results proved that the square texture had a superior friction performance. Later, they proposed a texture distribution based on a genetic algorithm. They discovered that asymmetric triangular/trapezoid texture distributions had a comparatively high bearing load and low friction [79]. Therefore, it can be seen from the above literature that the traditional arrangement had less effect than the non-standard arrangements. Furthermore, Ren et al. [84] investigated fishbone, sine, triangle, and honeycomb texture arrangements. Short groove textures with low area ratio sine arrangements improved the hydrodynamic pressure. At this time, the texture arrangement design study

has not reached a common result. Each study emphasizes different organizational forms and criteria, and there are few parameters that describe and characterize texture arrangement. While most researchers have focused on the texture arrangement, some studies have paid attention to the texture orientation's impact on the tribological performance.

The texture orientation can improve the hydrodynamic effect, raising the open force and minimizing the outflow [28,62]. Leakage is minimized when the texture is positioned at 0° and 90° in the flow direction but with a minimal effect on the hydrodynamic pressure. However, for a 40° – 70° orientation, there is a significant improvement in the load capacity, but the leakage remains high. Ding et al. [61] obtained an inclination angle of 0° of the elliptical dimples, which gives a lower friction coefficient, thereby enabling a stronger hydrodynamic effect. On the other hand, 60° was found to be the orientation with the maximum wear reduction [79]. A specific orientation of the texture can then result in a minimum contact area, thus improving the tribological behavior.

The effect of the arrangements can be improved further with the sliding direction. Some scientists [11,68,75], found that dimples with a distribution perpendicular to the reciprocating motion resulted in the production of a thicker film and a lower friction than those parallel to the sliding direction. In addition, for texture shapes such as the triangle or chevron, the orientation of the patterns to the sliding direction was significant in decreasing the friction when the side border perpendicular to the sliding motion first approached the region of contact [11]. However, the effect of the sliding direction on orientations may change [75]. Perpendicular grooves do not provide substantial tribological enhancements due to their huge transversal dimensions, and, when compared to untextured surfaces, parallel grooves reduced the performance of curved surfaces by increasing contact of the surfaces and the friction [3]. The reason might be that the similar orientation of the grooves to the sliding speed promotes lubricant flow inside the pattern, thereby preventing a pressure build-up of the local lubricant. For a chevron parallel to the sliding direction, a smaller angle of a chevron vertex between the chevron's arms can improve tribological behavior [11]. As a result, tribological properties may be highly sensitive to the geometric shape (concave or convex) and sliding conditions and, therefore, require more investigations.

4. Laser Surface Texture Processing Medium

The target material is melted, and its structure is altered during laser ablation in air. Material removal from the surface is related to the type of laser pulse parameters, as well as the material's thermal and optical properties [49,85–87]. The material ejected from the target surface forms a plasma plume, which expands and exits the target surface, producing a pressure wave that travels through the material's surface. The ejected material can redeposit on the surface, creating burrs and reducing the ablation efficiency. The hardness of these burrs or oxides is often higher than the original material's due to the oxidation effect, and elimination of these burrs is crucial for an optimum tribological behavior [41,85].

The physical, chemical, sand-blasting, acid, etching, and electropolishing burrs removal has been investigated. Although these methods provide positive outcomes, the substrate material is likely to be damaged, and the dimple size is likely to be affected. Using a liquid or gas is a great solution for improving ablation by reducing the thermal effect, burrs, and microcracks, as well as for maintaining the cleanliness of the mating surface [36,49,88]. Table 3 shows a synopsis of the studies on various ablation media. Processing media, such as liquids, gases, and others, will be reviewed in Section 4.

Table 3. Some studies on water ablation processing.

Materials	Processing Environment	Findings	Ref
Ti6Al4V	Air and water	Underwater ablation produced a better upper and bottom shape with an efficient control of laser parameters.	[89]
Crystalline Silicon	Air and water	The roughness of the textured surfaces was 7.2 μm in air and 5.5 μm in water.	[90]
Aluminum	Air and distilled water	Obvious bubble formation in water that led to control of the ablation rate.	[85]
—	Air and water	In water, there was an improvement in laser energy coupling to the target surface and more energy was delivered to the cavity's sidewalls.	[91]
Titanium	Flowing water	A uniform feature was achieved by combining a high laser pulse frequency with a large water flow speed.	[19]
Bone Tissue	Underwater	The bubble's hydrokinetic forces helped to reduce heat damage and improved the crater's geometry.	[92]
LCD glass, Alumina	Air and water	In comparison to air, underwater processing reduced microcracking and the heat-affected zone by the synergistic use of laser power and pulse repetition rate.	[93]
Stainless Steel			[94]
Ti6Al4V	Ethanol, saturated, sodium bicarbonate	The water contact angle and the rolling angle in the ethanol medium were 54.9° and 9.8°. Furthermore, the textured surface in the saturated sodium bicarbonate solution exhibited excellent water adhesion.	[49]
Al-Li Alloys	Argon or air	The cut-edge surfaces of air were gritty, and dross was visible at the bottom. Using argon, grooves were produced, and the range of cutting speeds was discovered with no dross.	[95]
Aluminum	Underwater	The drilling was most enhanced for a 3-mm thick water layer.	[87]

—: Not reported.

4.1. Pulse Laser Ablation Processing with Liquids

In order to overcome the drawbacks of laser ablation in the air, a solution was developed that included underwater ablation or water-assisted subtractive machining processes using the liquid layer, water droplet, and moving water approaches, as shown in Figure 5 [85–87,89,90,94,96]. Underwater processing is superior to in-air processing (Figure 6a) and helps to avoid the re-deposition of debris due to the flowing effect of water [91]. Metal melting and vaporization are reduced, and particle re-deposition are stopped, as seen in Figure 6b. However, as seen in Figure 6d, divergent refraction of the laser beam can reduce the size of the resultant hole.

Wee et al. [97] used a laser to target a silicon substrate under air and water. Water as a processing medium minimized spatters and reduced tapers with fewer nanoparticles and no cauliflower formation on the surface. In addition, using a flowing water system, Feng et al. [98] investigated multi-scan ablation for deep pattern construction on copper. They found that water reduced the heat-affected zone, and a continuous flow of water during the processing dissipated excess heat, particles, and bubbles more effectively than stagnant water. Water processing has the advantage of reducing burrs and improving the morphology of the crater as compared to laser ablation in air [89,93,99]. In Figure 7, the surface morphologies of the SiC ceramic microgrooves machined using air and water are illustrated. Undesirable effects, such as splash and debris residue on the kerf, emerged during air processing (Figure 7a), while, in water, a smooth surface of the microgrooves was obtained (Figure 7c), with essentially no deposited debris or recast layer. This is due to the optical breakdown that happens in water, resulting in vaporization, expansion, plasma shock wave, and gas bubbles that efficiently take away the accumulated debris [85,87,92,96]. However, when a liquid, such as oil, is vaporized, the resultant shockwave compresses the ablated molten metal targeted by the pulse, and the evaporation of the oil creates the

two aspects of gas (bubbles) and liquid, which can result in an unbalanced power intensity of the laser spot and a lower processing efficiency [88].

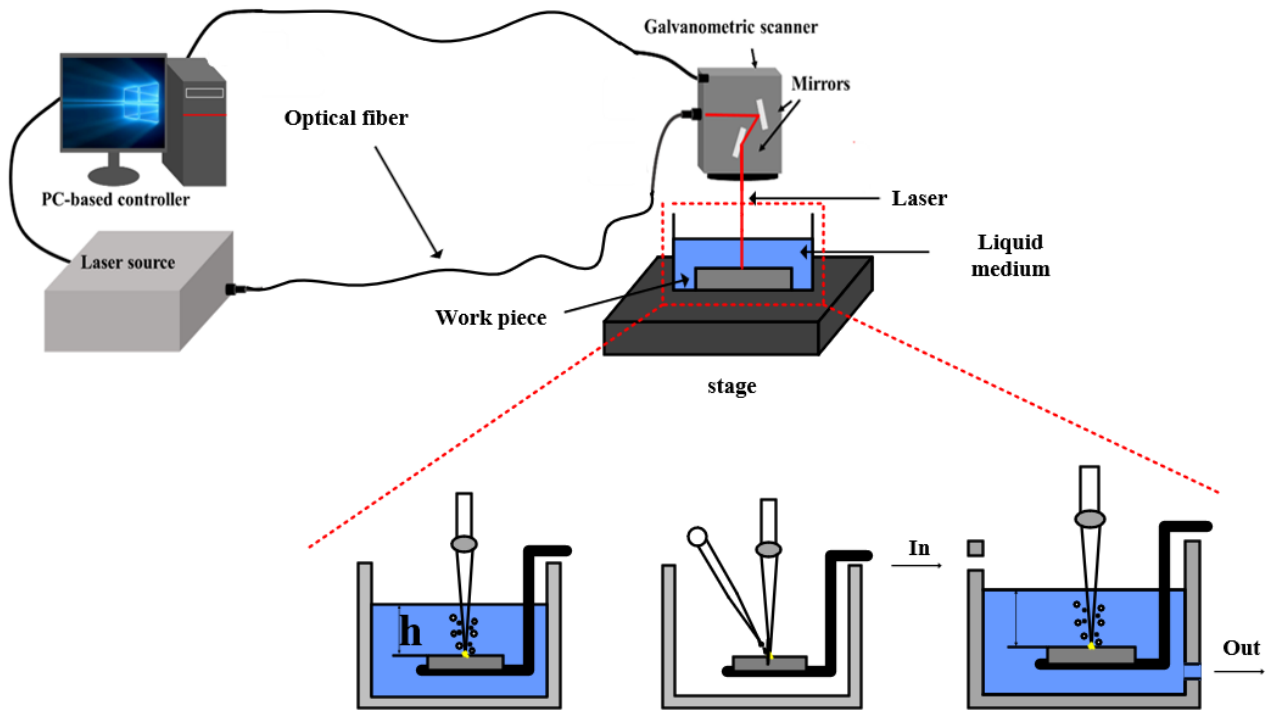


Figure 5. Experimental scheme of underwater laser ablation.

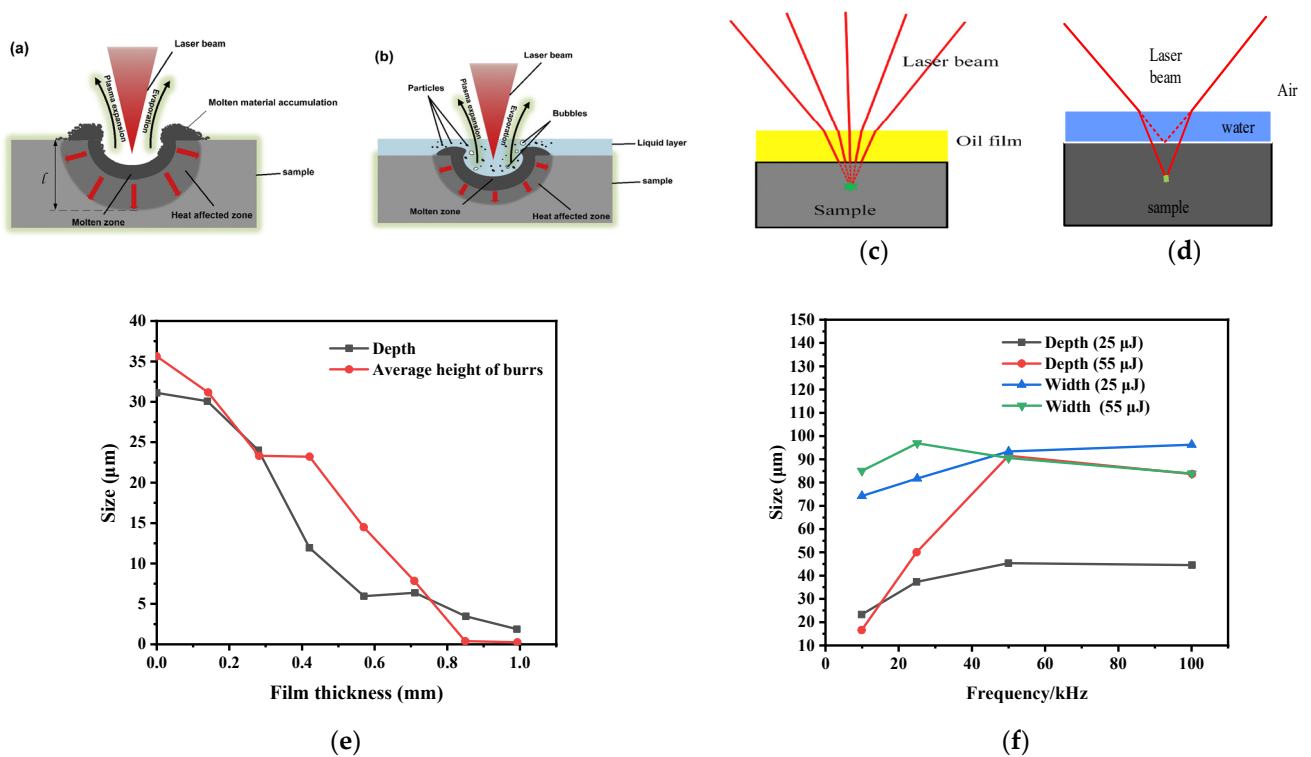


Figure 6. Cont.

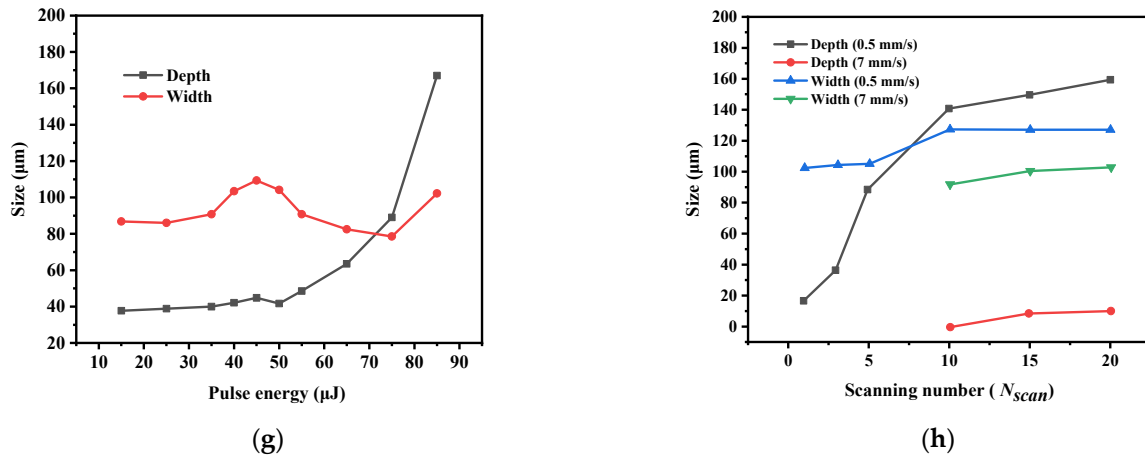


Figure 6. Schematic of laser ablation’s effect on the material: (a) in air; (b) with a liquid layer, reprinted with permission from [49], Copyright from Elsevier 2020; the change of the focus point induced by the optic effect of liquid layer; (c) in oil; (d) in water, reprinted with permission from [88,94], Copyright from Elsevier 2020, 2016; (e) ablation size volume of craters created on with oil film layer, reprinted with permission from [88], Copyright from Elsevier 2020; Sample depths and widths at various: (f) frequencies; (g) pulse energies; and (h) scanning numbers [100].

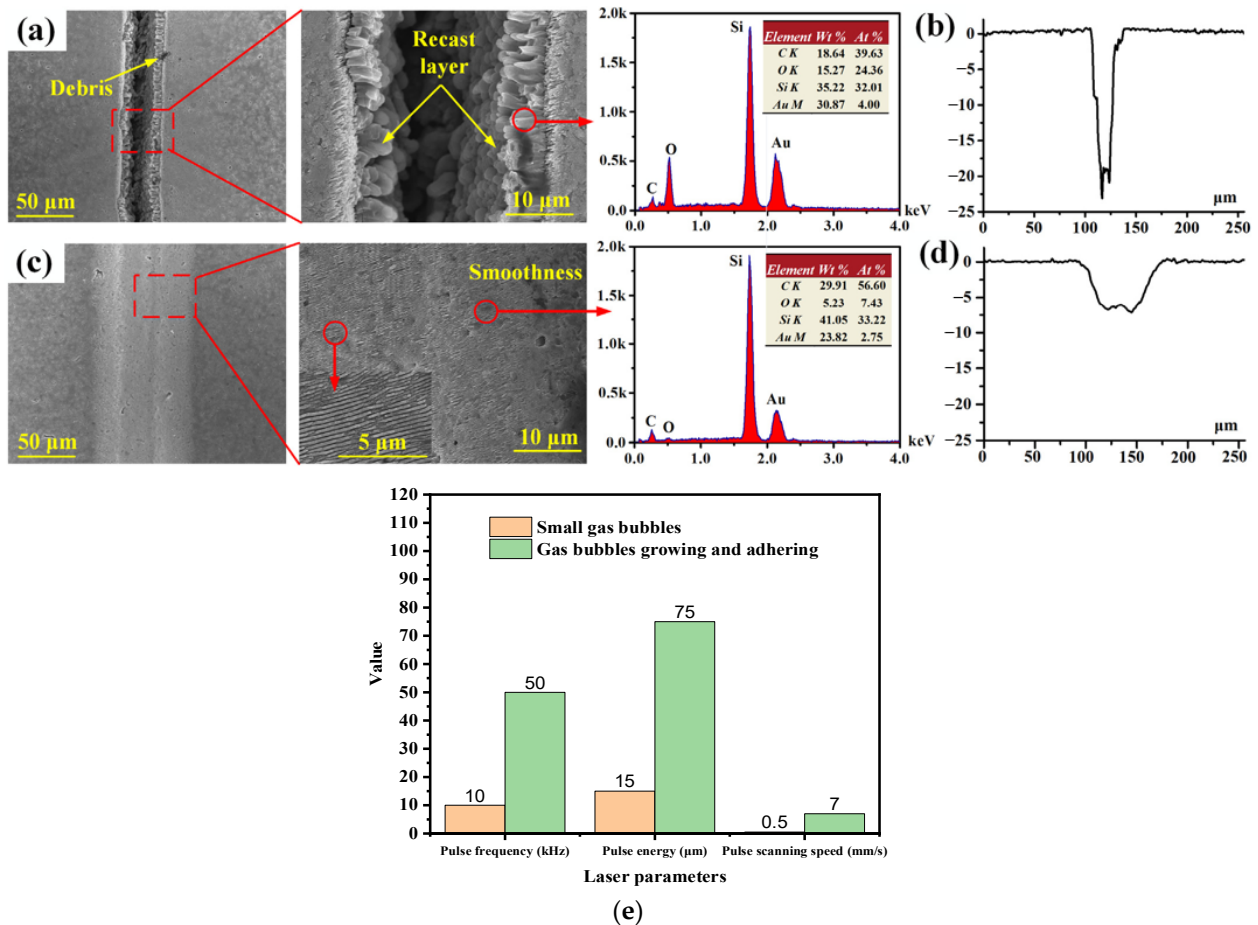


Figure 7. SEM image of generated hole: (a) in air; (c) in water, micro-pits’ cross-section profile (b) in air; (d) in water; (e) dynamic of bubble generation in underwater processing under various frequencies, pulse energies, and scanning speeds, adapted from [100].

Despite the positive benefits of underwater processing, including a uniform bottom profile [96], the effectiveness of water irradiation is less than that of air, since the targeted depth requires more repetitive scans [89]. In fact, while processing in water, a reduction in depth (Figure 7d) compared with the irradiation in air (Figure 7b) is noticed because of the water layer that limits the direct interaction of the laser with the surface. The crater size during underwater processing could be improved with proper selection of the water's film thickness, which is still challenging to define [87]. The change in the focal spot, induced by refraction (Figure 6c,d), can improve the width size but reduces the depth size (Figure 7d).

Laser parameters, including laser energy, laser frequency, the scanning speed, and the number of scans, have a substantial effect on the crater size [100,101]. The depth of the microgroove increased with a frequency between 10 and 50 kHz and a pulse energy of 25 μJ saturated, as shown in Figure 6f, and decreased at a 55 μJ pulse energy or a 100 kHz frequency. With 25 μJ , the width increased at 10 and 25 kHz, and then decreased at 55 and 100 kHz. The growing trend was slightly below 55 μJ , as seen in Figure 6g. The microgroove's depth grows quickly as the pulse energy increases, yet the microgroove's depth fluctuation becomes bigger. Due to the nonlinear impact of underwater laser processing, the microgroove's width increased with a pulse energy below 55 μJ and subsequently decreased with a pulse energy between 55 and 75 μJ . Figure 6h shows that when the number of scans increases, the microgroove's depth decreases. The width of the microgroove improves with the scanning number and speed. The laser parameters have an impact on the bubbles generated during processing, as illustrated in Figure 7e. When the conditions were a low pulse energy (15 μJ), low frequency (10 kHz), and low scanning speed (0.5 mm/s), disturbance-free removal was achieved. The gas bubbles were tiny and quickly evaporated at low values with no negative effect on the machining area. The gas bubbles moved in the opposite direction of the water. It was possible for the debris to be taken away, keeping the surface smooth. However, at a high frequency (50 kHz), laser energy (75 μJ), and scanning speed (7 mm/s), the phenomenon of a gas bubble explosion occurred, and the gas bubble clusters emerged abruptly, causing uncontrollable reflection, refraction, and scattering of the laser beam, changing the position and intensity of the beam, and, potentially, leading to a poorly finished surface and defects. The pulse frequency, energy, and scanning speed should be less than 50 kHz, 75 μJ , and 7 mm/s, respectively.

Oil has a stronger thermal resistance than water, and alcohol has a lower collapse limit than water, which could counter water's limitations as a medium [49,100,102,103]. Zhang et al. [88] used the oil processing medium to improve the processing quality and tribological properties of textured surfaces. Oil with a 0.28 mm thickness exhibited a remarkable cooling effect, preventing hot oxides from sticking to friction pairs. A thick oil film has a detrimental effect on crater size and generated burrs (Figure 6e). Furthermore, using a volatile solvent, such as ethanol or methanol, as a processing medium, improved the machining process by promoting burr-free holes, fewer cracks, no thermal damage, and a uniform shape with relatively quick evaporation of the alcohol. Ouyang et al. compared air, isopropanol, distilled water, and glycerin laser processing of Al and Ti alloys under ambient conditions [104]. The surface morphologies of the holes generated in glycerin were smooth with fewer burrs than those created in liquids because of its high viscosity. Furthermore, the density, thermal conductance, and acoustic impedance of the fluid medium affect the laser ablation efficiency. However, for laser ablation, additional liquid solutions, such as KOH, shielding oil, or grease, which have excellent oxygen-retardant qualities, might be used to improve ablation efficiency.

4.2. Pulse Laser Ablation Processing with Gases

Although liquid-assisted laser machining gives great results, it is not always effective because of the light absorption and scattering in liquids that are greater than in gases and some phenomena, including corrosion/oxidation, contamination of the workpiece with carbon, the collapse of bubbles, and defects [103]. It is then important to consider

gas-assisted laser ablation. Gases can act as oxidation retardants and can enhance the melt expulsion, spattering, and ejection of the molten material (Figure 8a–d) [95,105–107].

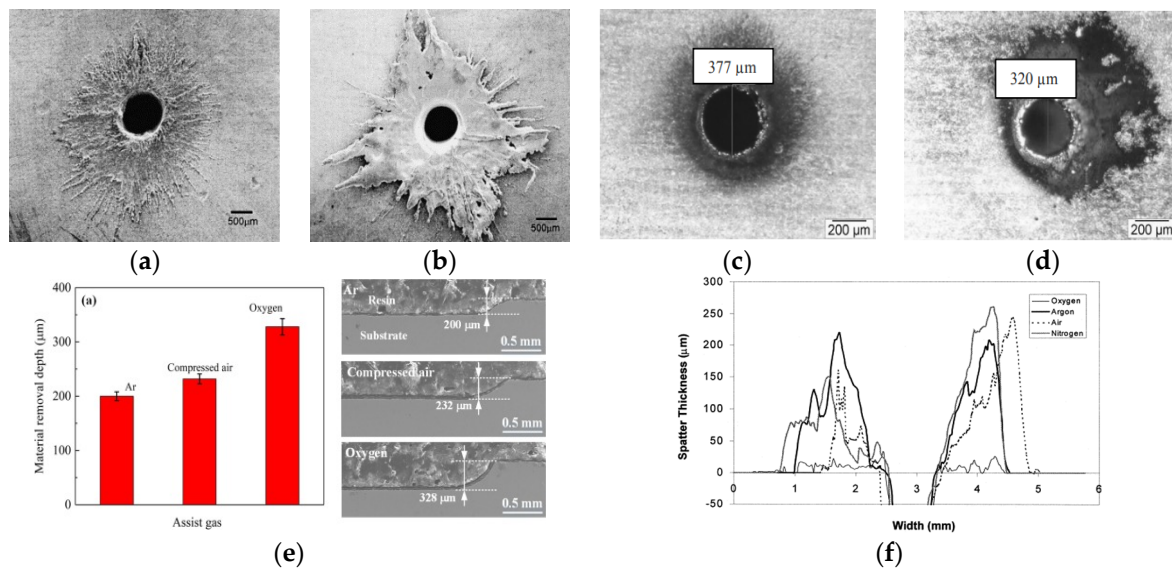


Figure 8. Typical measured spatter thickness geometry: (a) oxygen, (b) argon; (c) compressed air; (d) nitrogen, reprinted with permission from [106,107], copyright from Elsevier 2000, 2011; (e) material depth and cross-section shapes of laser etched with argon, compressed air, and oxygen, reprinted with permission from [36], copyright from Elsevier 2021; (f) spatter height with various gases, reprinted with permission from [106], copyright from Elsevier 2000.

Riveiro et al. [108] looked into the influence of an oxygen and nitrogen assist gas on the laser cutting of an Al-Cu alloy. Argon (Ar) was found to be the optimum candidate for a cutting-assistance gas. However, oxygen also proved to have a very great impact on the laser ablation performance (Figure 8e). In Figure 8a, with the oxygen assist gas, more material was ejected in the form of fragmented particles, and the vapor expulsion increased, resulting in few burrs on the surface. In addition, the image in Figure 8f showed that ablation with oxygen led to a smaller burr height compared to the other three assist gases. Oxygen and argon can then be employed in combination to speed up material removal at lower costs and to improve the textured surface quality and mechanical properties.

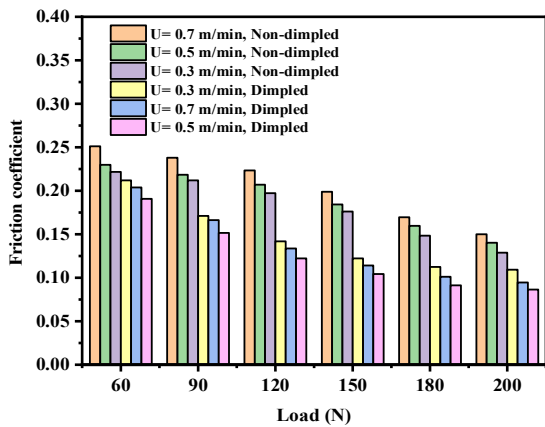
Recently, Xing et al. [36] compared three gases: argon, compressed air, and oxygen. It was observed that, despite argon's superior depth performance in the re-melted layer hardness, the usage of oxygen or compressed air showed a better laser ablation performance. Figure 8a,c clearly show the superiority of the ablation performance using oxygen and compressed air, respectively, over argon (Figure 8b) and nitrogen (Figure 8d). Furthermore, the region in which the ablated material re-deposits and the color of the re-deposit material are diverse when comparing the images in Figure 8b,d. It is gray for argon, while it is gray to black for nitrogen. Nitrogen has a bigger area of re-deposited material than argon. Exothermal chemical reactions on the material's surface decreased when gases or compressed air were used. As a result, the desired surface features were achieved.

However, ablation with an assist gas might occasionally result in poor stability. Thus, it is necessary to add another element that, in addition to the greater effect on gas flow, can also provide stability. Wang et al. [105] used an external longitudinal magnetic field to confine and guide laser-induced plasma by vertical squeezing and horizontal stretching. A greater longitudinal magnetic field proved useful for plasma confinement and guiding. Laser ablation using a gas medium is still not well investigated and requires a further study.

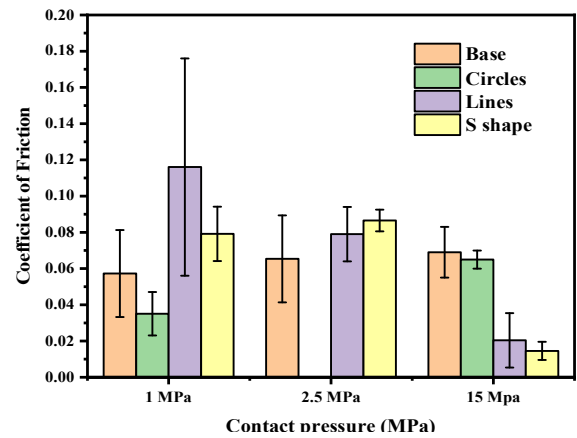
5. Effect of Surface Texture on Lubricated Condition

Different lift-generating processes are used to lubricate flat textured surfaces. However, the sliding pair's operating parameters depend on parameters such as the load and sliding frequency [109]. The mechanical pair is in a state of boundary lubrication when the sliding speed is low with a high load, which creates a monolayer of lubricant that covers the interacting surfaces [110] with contact asperities that increase the friction. For mixed lubrication ($1 < \lambda < 3$), the film thickness can support the load and reduce the contact asperity. Surface texture can generate microfluidic dynamic pressure, improve the contact state of the asperities, collect debris and lubricant, and reduce abrasive and adhesive wear [41,111]. In the hydrodynamic lubrication ($\lambda > 3$), the speed of pairs relative to the movement continues to increase. At this point, the texture under hydrodynamic pressure can fully support the load [112]. However, the potential of the oil pocket to store and release lubricants is the mechanism behind the improved tribological performance of the surface texture in a lubricated state. A surface texture's geometric features may be crucial for storing and releasing lubricants at different loads and sliding speeds [11,67,74,75,113–116]. As illustrated in Figure 9a, when compared to non-dimpled surfaces, the friction coefficient of the dimpled surfaces is reduced with higher loads and sliding speeds. In Figure 9b, under a low contact pressure, the circle exhibited the lowest COF, compared to that of the "S" shape and others. Under a higher contact pressure, the grooved texture (line and "S" shape) exhibited the lowest COF. However, traditional lubricants, particularly oils, are formed from natural hydrocarbon components and have a low thermal balance. They also deteriorate in hostile conditions, and, during operation, oil moves outside the friction interface. It is vital to replenish the lubricant in such a situation.

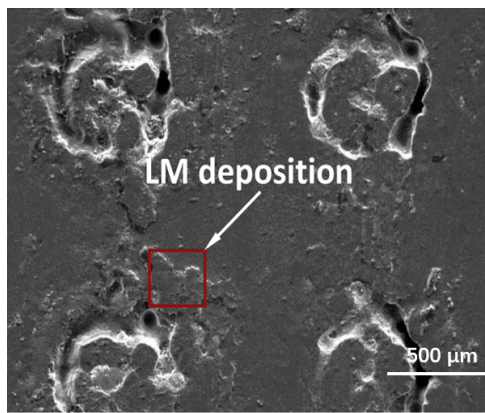
Liquid metal (LM) lubricants [81,117–119], nanoparticle oil lubricants [119–123], solid lubricants [32,124–131], and water lubricants [41,76,132–134] have all recently exhibited fascinating behavior in overcoming the traditional oil lubricants' limitations. The mechanisms of these lubricants can be shown in Figure 10. The lubrication mechanism of LM has been attributed to its interaction with the atmosphere [119–135], which results in the production of an oxide film in aerobic and of an adhesive film in anaerobic conditions (Figure 10). Liquid metal converting to a paste might easily adhere to the contact zone during the process, thereby lowering the COF and wear resistance. Liquid metal can act like a coating layer, protecting the mating surfaces from excessive wear. The wear scar in Figure 9c showed a very smooth surface with few wear debris, and the EDS in Figure 9d revealed a very strong concentration of Ga on the surface, showing LM adhesion on the tribo pair. Nanoparticles acting abrasively can support the load of the mating surface and transfer a tribo-film layer onto the mating surfaces in extreme conditions. The same mechanism can be attributed to solid lubricants, where a tiny lubricant layer can be formed at the interface; in addition, the release of the texture lubricant onto the contact surface improves the tribological behavior. As seen in Figure 11a, the average friction of the patterned samples burnished with CaF_2 or h-BN solid lubricants resulted in a high friction coefficient, compared to that of WS_2 or graphite solid lubricants for which it was relatively low. A similar result can be seen on the wear resistance (Figure 11b). The reason might be the ability of the solid lubricant to stick to and transfer a tribo-film onto the contact surface. Furthermore, the presence of water on a surface covered by textures could easily capture wear debris or chase the debris away from the contact area, with the water layer keeping the surface clean, supporting the load (Figure 11c) at a sufficient quantity, and decreasing the friction and wear.



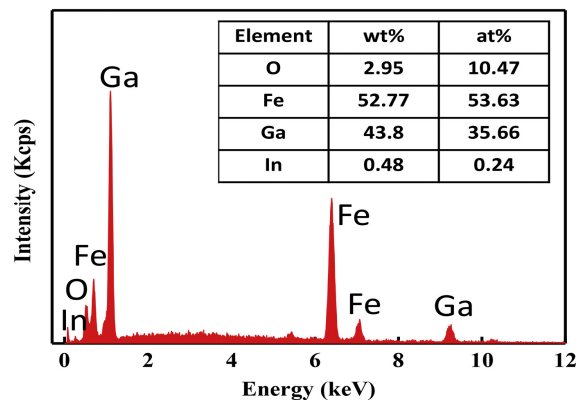
(a)



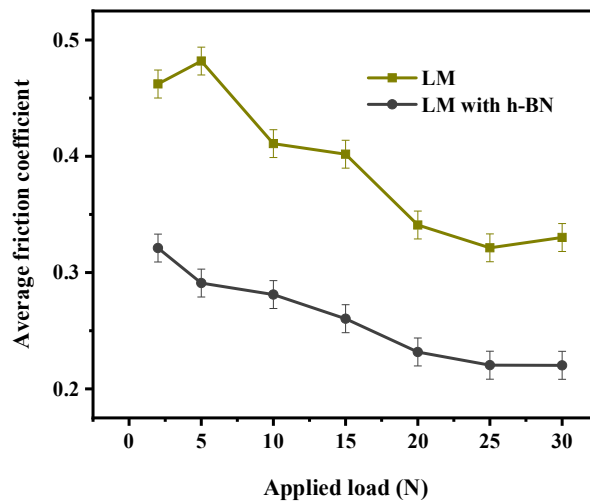
(b)



(c)



(d)



(e)

Figure 9. (a) the coefficient of friction with applied loads at distinct sliding velocities, reprinted with permission from [116], copyright from Elsevier 2010; (b) the COF with different texture geometries at 1 and 15 MPa, reprinted with permission from [67]. Copyright from Elsevier 2021; (c) SEM wear scar and LM deposition; (d) EDS evaluation of LM lubrication under extreme conditions of 10 N, 4 Hz, and 15% area density, reprinted with permission from [81], copyright from Elsevier 2019; (e) average friction with LM and LM with 8 wt% h-BN nanosheets under various applied loads, reprinted with permission from [119]. Copyright from Elsevier 2021.

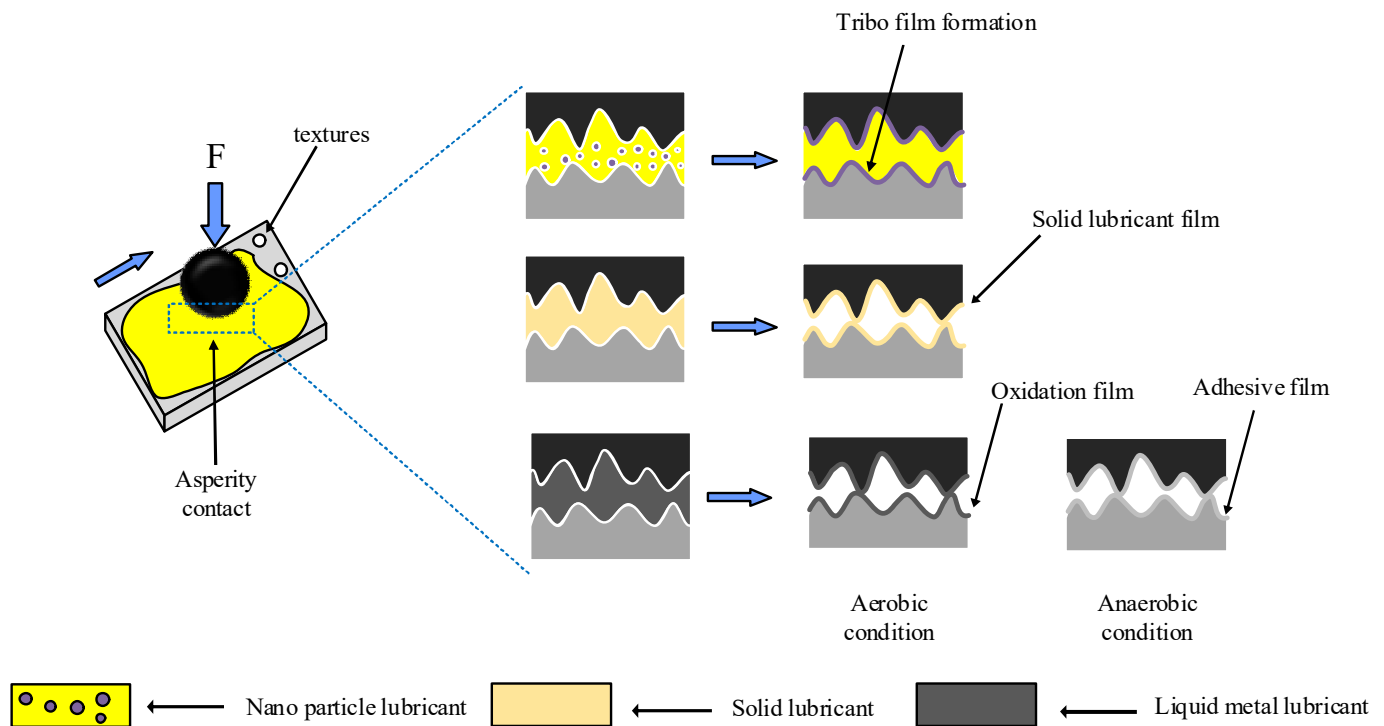


Figure 10. Schematic of the proposed lubrication mechanism of nanoparticle lubricants, solid lubricants, and liquid metal lubricants.

However, these new lubricants might be enhanced further with the use of additives. When coupled with the h-BN nano-additive [119], the tribological behavior of the LM lubrication yields extremely excellent tribological behavior under an extreme applied load, as seen in Figure 9e. In addition, for oil additives, Qi et al. [136] examined the synergistic lubricating impact of antioxidants and low-content ZDDP. According to the results, 2,6-Di-tert-butyl-4-methylphenol (BHT) antioxidant may increase ZDDP's anti-wear performance and the grease's anti-wear performance. However, the use of this low content ZDDP has not been tested on surface texture and might be beneficial for further enhancement of tribological properties. In addition, the h-BN nanosheet can be considered as a candidate for enhancing the friction and wear resistance, since it can readily shear at contact surfaces with the aid of its multi-layer crystal structure, which is comparable to graphene [119]. Furthermore, Fu et al. [125] focused on a modified WS₂ solid lubricant hot-pressed in texture. According to the results, the synergistic action of the textures and lubricant offered excellent anti-friction and anti-adhesion properties with a WS₂ release rate decreased by 102.2% by employing a silane coupling agent. More recently, Li et al. [137] has created a GuGa2 coating on copper-based materials, that utilizes the variation of gallium liquid metal surface tension. During the sliding process, the GuGa2 grains tended to compress smoothly and were capable of creating scratched tribo-film. Subsequently, on the worn surface, gallium, indium, and oxides helped reduce the friction and wear. As illustrated in Figure 11d, the synergistic influence of the 3-APS (3-aminopropyltriethoxysilane) treated in water lubricant and the surface texture further decreased the wear compared to the untextured and textured without 3-APS [138,139]. These newest lubricants and additives have shown tremendously positive results in enhancing the tribological performance. However, many of these lubricants have yet to be tested on surface texture. Table 4 demonstrates how different lubricants affect surface texture.

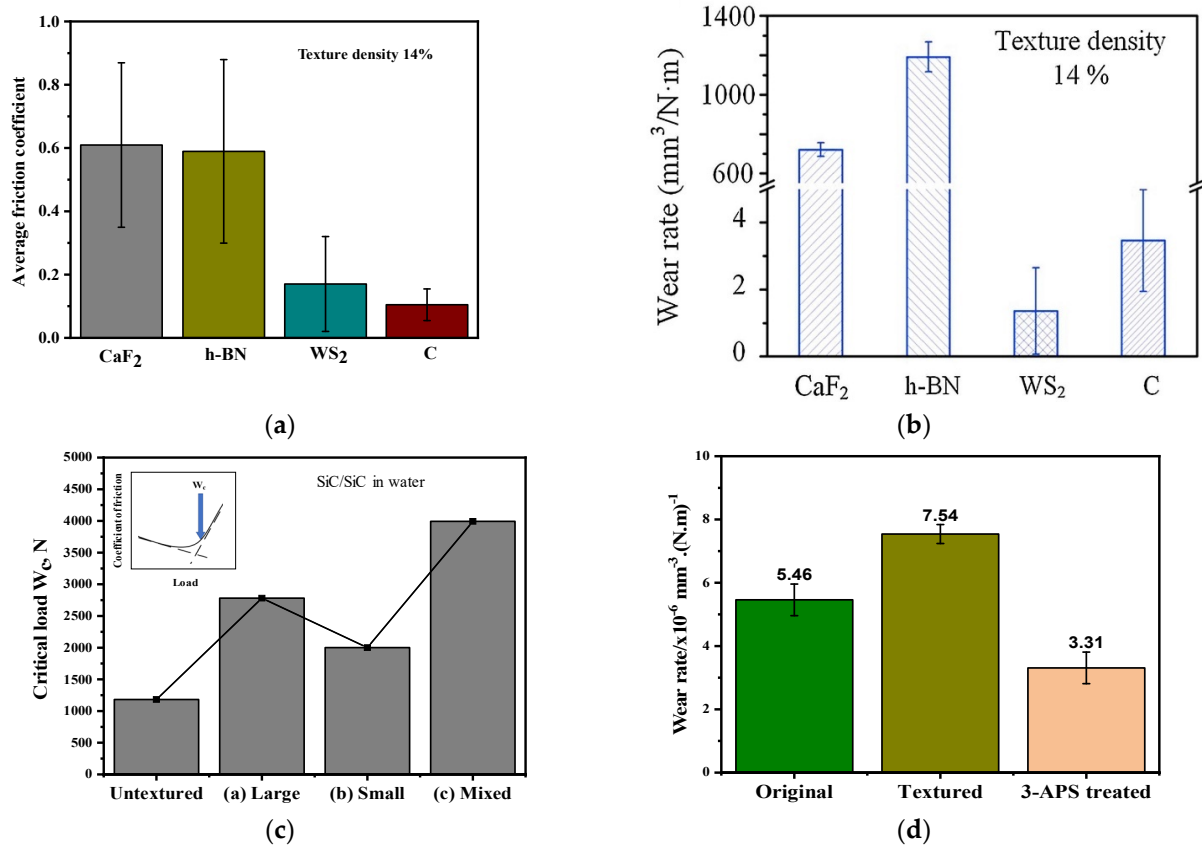


Figure 11. (a) COF and (b) wear rate of patterned surfaces burnished with CaF₂, h-BN, WS₂, and graphite solid lubricants, reprinted with permission from [127], copyright from Elsevier 2019; (c) Critical load of non-textured and textured samples, reprinted with permission from [132], copyright from Elsevier, 2006; (d) wear rates of different Al-bronze surfaces, reprinted with permission from [139], copyright from Elsevier, 2020.

Table 4. Effects of various lubricants on surface texture.

Type of Lubricants	Surface Texture	Observation	Ref
Water, oil	Micro grids	Friction was reduced by up to 27.64% for water lubrication compared to oil lubrication. Wear was reduced by up to 88.39% compared to water lubrication.	[41]
Water	Elliptical and groove textures	The groove surface texture exhibited lower friction and wear.	[99]
Graphene or MoS ₂ solid lubricant	Cross groove	For 18 and 40% area densities, graphene had a longer lifetime than MoS ₂ .	[128]
DLC coating	Dimple	Patterned chambers and the DLC covering increased the peak energy by approximately 5.8%.	[126]
ZDDP, DDP lubricants additives	—	It was found that under all conditions, the performance of ZDDP as an anti-wear film was superior to that of DDP.	[129]
Paraffin oil	Micro-grooved crosshatch	It has been discovered that each texture’s geometric parameter had an effect on friction.	[59]
Polyalphaolefin (PAO)	Dimple	The best dimple arrangement was hexagonal with a 10% area density and a 0.1 area ratio.	[82]
ZDDP	Dimple, cross	The cross patterns reduced the wear loss by two orders of magnitude via lubricant storage in the textured pockets and anti-wear tribo-film formation.	[110,130]

Table 4. Cont.

Type of Lubricants	Surface Texture	Observation	Ref
h-BN	—	An h-BN lamellae tribo-chemical thin layer on contact surfaces decreased friction and protected the contact interface.	[122,123]
MoS ₂	Multi-dimple pattern	The dimple combined with MoS ₂ increased tribological performance for most applied loads.	[131]
Sn-Ag-Cu	Groove	The groove-textured surfaces with 20 and 25% area densities filled with Sn-Ag-Cu solid lubricant had the lowest friction.	[124]
Seawater lubrication	Hemispherical, triangular, elliptical	The ellipsoidal pits had the highest frictional performance, followed by triangular pits; hemispherical pits had the poorest frictional performance.	[133]
Liquid metal droplet wrapped in chitosan (NLMWC) in water	—	NLMWC added in water reduced the friction and wear rate by 40% and 69%, respectively.	[134]

—: Not reported.

6. Application of Surface Texturing

Surface texturing has been widely used in a variety of elements, such as automobile engines; cutting tools; biomedical applications, including hip joint replacements and dental implants; etc., as shown in Figure 12. The application of surface textures will be reviewed in Section 6 in association to superhydrophobic surfaces as well as anti-drag and vibration and noise control in mechanical equipment.

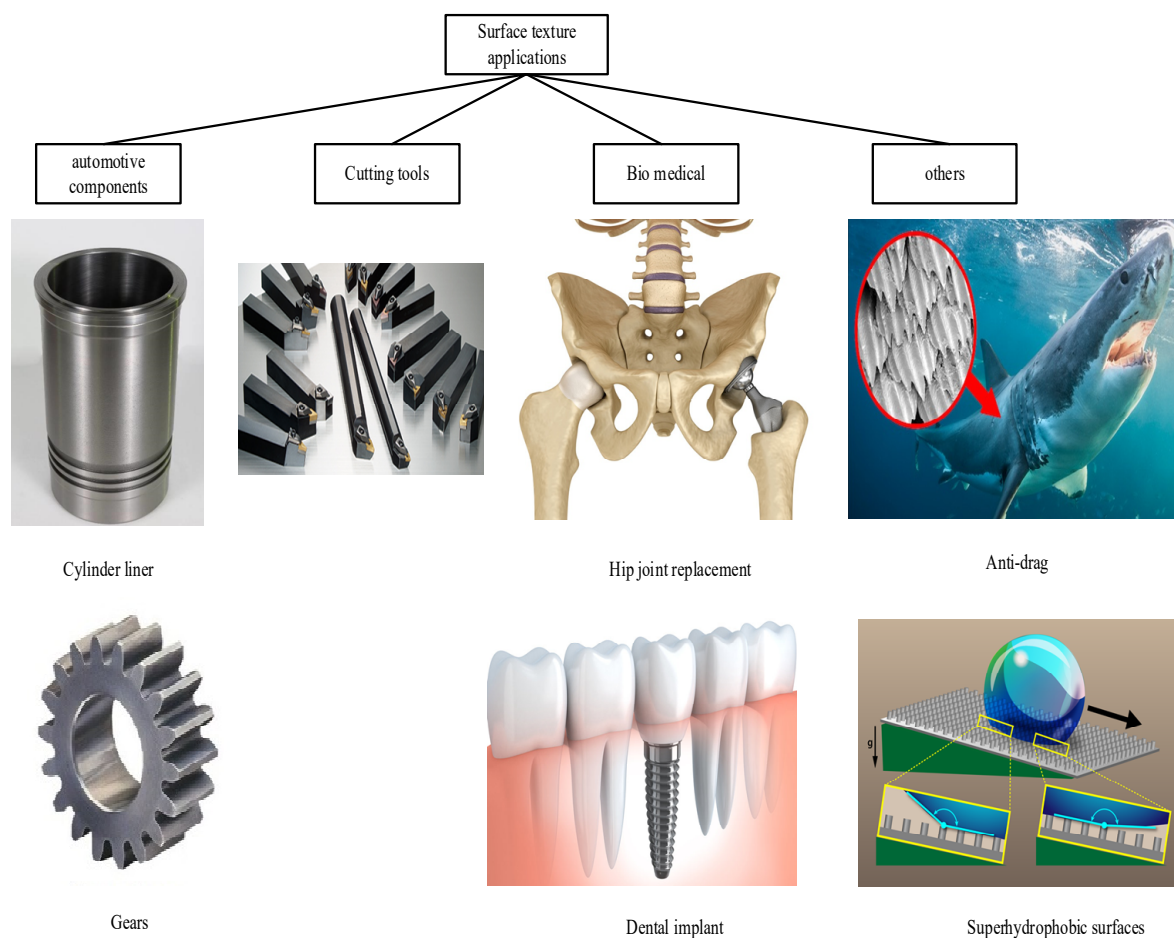


Figure 12. Application of surface texturing.

6.1. Surface Texture for Superhydrophobic Surfaces

Laser surface texturing using nanosecond, picosecond, and femtosecond laser techniques has been previously shown to be effective for the creation of superhydrophobic (SH) surfaces in various kinds of materials [48]. Superhydrophobic surfaces have outstanding water resistance characteristics and are non-wetting, anti-icing, dust/mud self-cleaning, and corrosion resistant [140] due to a contact angle greater than 150° . The nanosecond laser is the most commonly used technique to create superhydrophobic surfaces because of its efficient and less expensive procedure that can process data significantly faster, turning the surface from hydrophobic to superhydrophobic when exposed to ambient circumstances [141–143]. However, the fabrication of a durable and repairable superhydrophobic surface often requires additional chemical treatment. Ma et al. [48] used the nanosecond laser to fabricate a succession of circle-shaped texture patterns with various pitches over diameter values (p/d). The hydrophobicity was obtained not only after additional chemical modification but also with the p/d value. In addition, Wang et al. [49] obtained a contact angle of 154.9° with ethanol solution, indicating that the surface was SH, followed by the bicarbonate solution. Even after ambient air exposure, the superhydrophobicity persisted.

SH surfaces require an adequate surface morphology; it is vital to control the surface topology. Authors have been frequently inspired by nature while creating such surfaces. Fabricating a superhydrophobic surface on metal materials, inspired by lotus leaves, offers a lot of potential for corrosion prevention [144,145]. Surface texture is an efficient way to create superhydrophobic surfaces, although chemical treatments to increase the superhydrophobicity and anti-fouling performances of textured surfaces are becoming increasingly common.

6.2. Surface Texture for Anti-Drag Application

The notion of resistance has caused a great impact on human life, using a lot of energy and resources in various applications, including ship navigation, water transportation, oil and gas pipelines, and microfluidic channels [146]. A reduced resistance can aid in increasing cruising speed and lowering fuel consumption [147,148]. Anti-drag surfaces are an excellent approach for reducing the resistance force between liquid and solid surfaces especially for superhydrophobic surfaces. Shark skin, dolphin skin, penguin feather-induced microbubbles, the “lotus effect” superhydrophobic, and the pitcher plant-inspired slippery drag reduction are just a few of the studies that have been done to solve the problem using a biomimetic approach [149]. However, shark skin is one of the biomimetic approaches with the most significant improvements, especially to turbulent flow. Many approaches have been used to mimic the shark skin riblet structure for drag reduction, including LST and 3D printing, with incredible results [149–152]. Controlling the geometric characteristics of patterns has a significant influence on a surface’s anti-drag properties [150–153]. Hydrophobic surfaces offer a lot of potential for reducing surface drag, especially in laminar flow [146]. Although numerical and experimental studies on anti-drag surfaces have been conducted, some limitations remain to be addressed, such as the use of a complete structure for an analysis of the drag reduction performance, superhydrophobic surfaces that can withstand high pressure, and in vivo methods for exploring the underlying mechanisms.

6.3. Surface Texture for Vibration and Noise in Mechanical Equipment

Noise at a low frequency (0–500 Hz) and noise at a high frequency (500–18,000 Hz) are two types of noise produced by friction, and these are directly caused by factors such as load, velocity, and shape of the surface [154]. Surface texture can be regarded as a potential solution to the problem of friction-induced noise, as vibrations and noises induced by friction are mostly determined by the contact state. The groove surface texture, for example, may effectively modify the interface’s contact state and interrupt the persistence of friction, thereby reducing and suppressing self-excited noise and vibration during the friction operation [154–156].

In order to get the best results, the oil pockets' design is of the utmost importance. By manipulating the geometric parameters of surface texture, vibration and noise can be suspended. Furthermore, several studies have demonstrated that lubricants can diminish the discontinuous contact state on the surface, thereby reducing the contact stress and strengthening the noise reduction effect. In this regard, the novel trend of combining textural and solid lubricants has recently showed tremendous promise [154,155,157,158]. Xue et al. [155] combined groove patterns and Sn–Ag–Cu solid lubricants. Friction leading to noise and vibration was suppressed with the formation of a CASs profile with visible wrinkles.

7. Conclusions and Outcomes

In the present review, the laser's interaction with the material, the texture's design characteristics, the processing media's influence on the ablation efficiency, and the operating parameters' impact on lubrication, as well as the optimized lubrication mechanism of some potential lubricants, were presented. From the discussion above, some conclusions can be drawn:

1. Depending on the material and the machining instrument, different pulse durations (ns, fs, and ps) have different effects. The ablation of 50CrMo4 steel required 1.5 W for the fs laser, 13.5 W for the ps laser, and >90 W for the ns laser. For silicon nitride, 1 W was required for the ps laser, with a maximum of 3 and 1.6 W for the ns laser. A lower pulse power lowered the HAZ and created burrs in both situations. Short and ultra-short lasers can withstand a high laser power while causing less heat damage and defects.
2. Low scanning speeds (less than 10 mm/s) provide high-quality surface textures in a wide range of materials, but high scanning speeds may result in smaller widths and deeper depths. A high repetition rate could reduce the size and volume of craters.
3. Using an assist processing medium, such as a liquid or gas, can enhance crater structure, eliminate microcracks and debris redeposition, and reduce HAZ. The accumulation of fatigue on the target surface can be caused by ionization of water, recurrent high pressure, and thermal stress. The laser-induced gas bubble might scatter the laser beam, compromising the treated surface's accuracy. Alcohol solution, KOH, or a shielding oil can be used to avoid gas bubbles and oxidation, thereby improving the surface's finish. There are few investigations of laser ablation with a gas medium; this might be a future study subject.
4. The texture characteristics have an indisputable effect on the tribological performance of mechanical equipment. The area density and area ratio are critical characteristics that have a significant impact on the tribological performance, with the area density affecting the performance in the range of 5%–20% and the area ratio less than 1. The design parameters should be carefully selected to ensure the generation of a thick lubricating film, lubricant storage, release, and a self-lubricating system.
5. Oil lubricant is made of natural hydrocarbon elements that have low thermal stability, degrade quickly, and can move outside the friction contact when subjected to higher loads and sliding frequencies. The introduction of new lubricants provides a clear mechanism for the friction and wear reduction in extreme conditions. Furthermore, the synergistic usage of the surface texture and coating in the case of solid lubricants can increase the tribological behavior.

Despite LST's rapid advancement, there are presently no guidelines or criteria for controlling the design of surface textures, particularly for real-world applications, because of the additional manufacturing steps and costs to the industry. The trial-and-error method is still the most popular, although it has limitations with regard to texturing performance. Furthermore, no appropriate theoretical model for predicting the experimental tests has been found. As a result, a future focus could be on numerical approaches, such as machine learning. Indeed, the large number of studies on surface texture can help in the development of a predictive model that uses artificial intelligence to predict the impact of laser parameters, texture designs, and lubricants on tribological properties, allowing for the

selection of the best texture layout and working conditions prior to the manufacturing process. Furthermore, self-lubricating devices might be seen as an innovative way to improve the tribological performances of mechanical equipment. This review can serve as a reference for current investigations and future perspectives on LST technology for the design and operation of mechanical components.

Funding: This work was financially supported by the National Natural Science Foundation of China (No. 51975454).

Institutional Review Board Statement: Not applicable.

Informed Consent Statement: Not applicable.

Data Availability Statement: Not applicable.

Conflicts of Interest: The authors declare no conflict of interest.

References

1. Todhunter, L.D.; Leach, R.K.; Lawes, S.D.A.; Blateyron, F. Industrial survey of ISO surface texture parameters. *CIRP J. Manuf. Sci. Technol.* **2017**, *19*, 84–92. [[CrossRef](#)]
2. Macek, W. Fracture surface formation of notched 2017A-T4 aluminium alloy under bending fatigue. *Int. J. Fract.* **2022**, *234*, 141–157. [[CrossRef](#)]
3. Boidi, G.; Grutmacher, P.G.; Kadiric, A.; Profito, F.J.; Machado, I.F.; Gachot, C.; Dini, D. Fast laser surface texturing of spherical samples to improve the frictional performance of elasto-hydrodynamic lubricated contacts. *Friction* **2021**, *9*, 1227–1241. [[CrossRef](#)]
4. Akbarzadeh, A.; Khonsari, M.M. Effect of Untampered Plasma Coating and Surface Texturing on Friction and Running-in Behavior of Piston Rings. *Coatings* **2018**, *8*, 110. [[CrossRef](#)]
5. Rosenkranz, A.; Grutmacher, P.G.; Gachot, C.; Costa, H.L. Surface Texturing in Machine Elements—A Critical Discussion for Rolling and Sliding Contacts. *Adv. Eng. Mater* **2019**, *21*, 1900194. [[CrossRef](#)]
6. Etsion, I.; Burstein, L. A model for mechanical seals with regular microsurface structure. *Tribol. Trans.* **1996**, *39*, 677–683. [[CrossRef](#)]
7. Costa, H.; Hutchings, I. Some innovative surface texturing techniques for tribological purposes. *Proc. Inst. Mech. Eng. Part J J. Eng. Tribol.* **2015**, *229*, 429–448. [[CrossRef](#)]
8. Roy, T.; Choudhury, D.; Mamat, A.B.; Pingguan-Murphy, B. Fabrication and characterization of micro-dimple array on Al₂O₃ surfaces by using a micro-tooling. *Ceram. Int.* **2014**, *40*, 2381–2388. [[CrossRef](#)]
9. Lee, H.; Yi, A.; Choi, J.; Ko, D.H.; Kim, H.J. Texturing of polydimethylsiloxane surface for anti-reflective films with super-hydrophobicity in solar cell application. *Appl. Surf. Sci.* **2022**, *584*, 152625. [[CrossRef](#)]
10. Chatterjee, S.; Shariff, S.M.; Majumdar, J.D.; Choudhury, A.R. Development of nano-structured Al₂O₃-TiB₂-TiN coatings by combined SHS and laser surface alloying. *Int. J. Adv. Manuf. Technol.* **2008**, *38*, 938–943. [[CrossRef](#)]
11. Wos, S.; Koszela, W.; Pawlus, P. Comparing tribological effects of various chevron-based surface textures under lubricated unidirectional sliding. *Tribol. Int.* **2020**, *146*, 106205. [[CrossRef](#)]
12. Guo, Y.B.; Caslaru, R. Fabrication and characterization of micro dent arrays produced by laser shock peening on titanium Ti-6Al-4V surfaces. *J. Mater. Process. Technol.* **2011**, *211*, 729–736. [[CrossRef](#)]
13. Kovalchenko, A.; Ajayi, O.; Erdemir, A.; Fenske, G.; Etsion, I. The effect of laser surface texturing on transitions in lubrication regimes during unidirectional sliding contact. *Tribol. Int.* **2005**, *38*, 219–225. [[CrossRef](#)]
14. Bieda, M.; Schmadicke, C.; Roch, T.; Lasagni, A. Ultra-Low Friction on 100Cr6-Steel Surfaces After Direct Laser Interference Patterning. *Adv. Eng. Mater.* **2015**, *17*, 102–108. [[CrossRef](#)]
15. Costil, S.; Lamraoui, A.; Langlade, C.; Heintz, O.; Oltra, R. Surface modifications induced by pulsed-laser texturing—Influence of laser impact on the surface properties. *Appl. Surf. Sci.* **2014**, *288*, 542–549. [[CrossRef](#)]
16. Cernasejus, O.; Skamat, J.; Markovic, V.; Visniakov, N.; Indrisiunas, S. Effect of Laser Processing on Surface Properties of Additively Manufactured 18-Percent Nickel Maraging Steel Parts. *Coatings* **2020**, *10*, 600. [[CrossRef](#)]
17. Trucchi, D.M.; Bellucci, A.; Girolami, M.; Mastellone, M.; Orlando, S. Surface Texturing of CVD Diamond Assisted by Ultrashort Laser Pulses. *Coatings* **2017**, *7*, 185. [[CrossRef](#)]
18. Maharjan, N.; Zhou, W.; Zhou, Y.; Guan, Y.C.; Wu, N.E. Comparative study of laser surface hardening of 50CrMo4 steel using continuous-wave laser and pulsed lasers with ms, ns, ps and fs pulse duration. *Surf. Coat. Technol.* **2019**, *366*, 311–320. [[CrossRef](#)]
19. Tangwarodomnukun, V. Cavity formation and surface modeling of laser milling process under a thin-flowing water layer. *Appl. Surf. Sci.* **2016**, *386*, 51–64. [[CrossRef](#)]
20. SHsu, M.; Jing, Y.; Hua, D.; Zhang, H. Friction reduction using discrete surface textures: Principle and design. *J. Phys. D Appl. Phys.* **2014**, *47*, 335307. [[CrossRef](#)]
21. Lu, L.B.; Zhang, Z.; Guan, Y.C.; Zheng, H.Y. Comparison of the effect of typical patterns on friction and wear properties of chromium alloy prepared by laser surface texturing. *Opt. Laser Technol.* **2018**, *106*, 272–279. [[CrossRef](#)]

22. Xu, X.J.; van der Zwaag, S.; Xu, W. The effect of martensite volume fraction on the scratch and abrasion resistance of a ferrite-martensite dual phase steel. *Wear* **2016**, *348*, 80–88. [[CrossRef](#)]
23. Trevisiol, C.; Jourani, A.; Bouvier, S. Effect of martensite volume fraction and abrasive particles size on friction and wear behaviour of a low alloy steel. *Tribol. Int.* **2017**, *113*, 411–425. [[CrossRef](#)]
24. Lu, P.; Wood, R.J.K.; Gee, M.G.; Wang, L.; Pflöging, W. A Novel Surface Texture Shape for Directional Friction Control. *Tribol. Lett.* **2018**, *66*, 51. [[CrossRef](#)]
25. Zhang, H.; Zhang, D.Y.; Hua, M.; Dong, G.N.; Chin, K.S. A Study on the Tribological Behavior of Surface Texturing on Babbitt Alloy under Mixed or Starved Lubrication. *Tribol. Lett.* **2014**, *56*, 305–315. [[CrossRef](#)]
26. Gu, C.X.; Meng, X.H.; Xie, Y.B.; Yang, Y.M. Effects of surface texturing on ring/liner friction under starved lubrication. *Tribol. Int.* **2016**, *94*, 591–605. [[CrossRef](#)]
27. Rosenkranz, A.; Costa, H.L.; Profito, F.; Gachot, C.; Medina, S.; Dini, D. Influence of surface texturing on hydrodynamic friction in plane converging bearings—An experimental and numerical approach. *Tribol. Int.* **2019**, *134*, 190–204. [[CrossRef](#)]
28. Hingawe, N.D.; Bhore, S.P. Tribological performance of a surface textured meso scale air bearing. *Ind. Lubr. Tribol.* **2020**, *72*, 599–609. [[CrossRef](#)]
29. Hu, S.; Zheng, L.; Guo, Q.G.; Ren, L.Q. Influence of Cross-Grooved Texture Shape on Tribological Performance under Mixed Lubrication. *Coatings* **2022**, *12*, 305. [[CrossRef](#)]
30. Sun, S.N.; Long, R.S.; Jin, Z.H.; Zhang, Y.M.; Ju, Z.C.; Du, X.Y. Research on the Friction and Wear Properties of Dents Textured Rolling Element Bearings under Dry Wear. *Coatings* **2022**, *12*, 684. [[CrossRef](#)]
31. Profito, F.J.; Vladescu, S.C.; Reddyhoff, T.; Dini, D. Transient experimental and modelling studies of laser-textured micro-grooved surfaces with a focus on piston-ring cylinder liner contacts. *Tribol. Int.* **2017**, *113*, 125–136. [[CrossRef](#)]
32. Ma, Z.; Song, J.J.; Fan, H.Z.; Hu, T.C.; Hu, L.T. Preparation and Study on Fretting Tribological Behavior of Composite Lubrication Structure on the Titanium Alloy Surface. *Coatings* **2022**, *12*, 332. [[CrossRef](#)]
33. Grutmacher, P.G.; Rosenkranz, A.; Szurdak, A.; Konig, F.; Jacobs, G.; Hirt, G.; Mücklich, F. From lab to application—Improved frictional performance of journal bearings induced by single- and multi-scale surface patterns. *Tribol. Int.* **2018**, *127*, 500–508. [[CrossRef](#)]
34. Grutmacher, P.G.; Rosenkranz, A.; Szurdak, A.; Gruber, M.; Gachot, C.; Hirt, G.; Mücklich, F. Multi-scale surface patterning—An approach to control friction and lubricant migration in lubricated systems. *Ind. Lubr. Tribol.* **2019**, *71*, 1007–1016. [[CrossRef](#)]
35. Ahmed, N.; Rafaqat, M.; Pervaiz, S.; Umer, U.; Alkhalefa, H.; Shar, M.A.; Mian, S.H. Controlling the material removal and roughness of Inconel 718 in laser machining. *Mater Manuf Process.* **2019**, *34*, 1169–1181. [[CrossRef](#)]
36. Li, X.; Arthanari, S.; Guan, Y.C.; Ramakrishna, S. Influence of assist gas on surface quality and microstructure development of laser metal processing. *Opt. Laser Technol.* **2021**, *143*, 107310. [[CrossRef](#)]
37. Bharatish, A.; Harish, V.; Bathe, R.N.; Senthilselvan, J.; Soundarapandian, S. Effect of scanning speed and tin content on the tribological behavior of femtosecond laser textured tin-bronze alloy. *Opt. Laser Technol.* **2018**, *108*, 17–25. [[CrossRef](#)]
38. He, X.; Zhong, L.; Wang, G.R.; Liao, Y.; Liu, Q.Y. Tribological behavior of femtosecond laser textured surfaces of 20CrNiMo/beryllium bronze tribo-pairs. *Ind. Lubr. Tribol.* **2015**, *67*, 630–638. [[CrossRef](#)]
39. Jia, Z.Y.; Ye, T.; Ma, J.W.; Cao, X.K.; Liu, W.; Yu, W.J.; Gao, J. Effect of Process Parameters on the Hardness of Laser Surface Textured 5A06 Aluminum Alloy. *J. Mater. Eng. Perform.* **2021**, *30*, 5858–5867. [[CrossRef](#)]
40. Soltani, B.; Azarhoushang, B.; Zahedi, A. Laser ablation mechanism of silicon nitride with nanosecond and picosecond lasers. *Opt. Laser Technol.* **2019**, *119*, 105644. [[CrossRef](#)]
41. Huang, J.Y.; Guan, Y.C.; Ramakrishna, S. Tribological behavior of femtosecond laser-textured leaded brass. *Tribol. Int.* **2021**, *162*, 107115. [[CrossRef](#)]
42. Zhang, J.J.; Yang, D.H.; Song, C.W.; Yan, Y.D.; Sun, T. Effect of pulse duration on tribological behavior of textured stainless steel by laser surface texturing. In Proceedings of the Asia International Conference on Tribology 2018, Kuching, Malaysia, 17 September 2018; *Asiatrib* 2018; pp. 8–10.
43. Gedvilas, M.; Indrišiusas, S.; Voisiat, B.; Stankevičius, E.; Selskis, A.; Raciukaitis, G. Nanoscale thermal diffusion during the laser interference ablation using femto-, pico-, and nanosecond pulses in silicon. *Phys. Chem. Chem. Phys.* **2018**, *20*, 12166–12174. [[CrossRef](#)] [[PubMed](#)]
44. Garasz, K.; Tański, M.; Kocik, M.; Iordanova, E.; Yankov, G.; Karatodorov, S.; Grozeva, M. The Effect of Process Parameters in Femtosecond Laser Micromachining. *Bulg. J. Phys.* **2016**, *43*, 110–120.
45. Mroczkowska, K.M.; Dzienny, P.; Budnicki, A.; Antonczak, A.J. Corrosion Resistance of AISI 304 Stainless Steel Modified Both Femto- and Nanosecond Lasers. *Coatings* **2021**, *11*, 592. [[CrossRef](#)]
46. Pou-Alvarez, P.; Riveiro, A.; Novoa, X.R.; Fernandez-Arias, M.; del Val, J.; Comesana, R.; Boutinguiza, M.; Lusquinos, F.; Pou, J. Nanosecond, picosecond and femtosecond laser surface treatment of magnesium alloy: Role of pulse length. *Surf. Coat. Technol.* **2021**, *427*, 127802. [[CrossRef](#)]
47. Shaheen, M.E.; Gagnon, J.E.; Fryer, B.J. Studies on laser ablation of silicon using near IR picosecond and deep UV nanosecond lasers. *Opt. Laser Eng.* **2019**, *119*, 18–25. [[CrossRef](#)]
48. Ma, Q.; Tong, Z.; Wang, W.; Dong, G.N. Fabricating robust and repairable superhydrophobic surface on carbon steel by nanosecond laser texturing for corrosion protection. *Appl. Surf. Sci.* **2018**, *455*, 748–757. [[CrossRef](#)]

49. Wang, Y.T.; Zhao, X.Y.; Ke, C.J.; Yu, J.; Wang, R. Nanosecond laser fabrication of superhydrophobic Ti6Al4V surfaces assisted with different liquids. *Colloid Interface Sci. Commun.* **2020**, *35*, 100256. [[CrossRef](#)]
50. Yu, Z.; Hu, J.; Li, K.M. Investigating the multiple-pulse drilling on titanium alloy in picosecond laser. *J. Mater. Process. Technol.* **2019**, *268*, 10–17. [[CrossRef](#)]
51. Liu, Q.; Liu, Y.; Li, X.; Dong, G.N. Pulse laser-induced cell-like texture on surface of titanium alloy for tribological properties improvement. *Wear* **2021**, *477*, 203784. [[CrossRef](#)]
52. Allahyari, E.; Nivas, J.J.; Avallone, G.; Valadan, M.; Singh, M.; Granata, V.; Cirillo, C.; Vecchione, A.; Bruzzese, R.; Altucci, C.; et al. Femtosecond laser surface irradiation of silicon in air: Pulse repetition rate influence on crater features and surface texture. *Opt. Laser Technol.* **2020**, *126*, 106073. [[CrossRef](#)]
53. Salguero, J.; del Sol, I.; Vazquez-Martinez, J.M.; Schertzer, M.J.; Iglesias, P. Effect of laser parameters on the tribological behavior of Ti6Al4V titanium microtextures under lubricated conditions. *Wear* **2019**, *426*, 1272–1279. [[CrossRef](#)]
54. Zhang, J.Y.; Long, Y.; Liao, S.X.; Lin, H.T.; Wang, C.Y. Effect of laser scanning speed on geometrical features of Nd:YAG laser machined holes in thin silicon nitride substrate. *Ceram. Int.* **2017**, *43*, 2938–2942. [[CrossRef](#)]
55. Allahyari, E.; Nivas, J.J.; Valadan, M.; Fittipaldi, R.; Vecchione, A.; Parlato, L.; Bruzzese, R.; Altucci, C.; Amoroso, S. Plume shielding effects in ultrafast laser surface texturing of silicon at high repetition rate in air. *Appl. Surf. Sci.* **2019**, *488*, 128–133. [[CrossRef](#)]
56. Sedao, X.; Lenci, M.; Rudenko, A.; Faure, N.; Pascale-Hamri, A.; Colombier, J.P.; Maclair, C. Influence of pulse repetition rate on morphology and material removal rate of ultrafast laser ablated metallic surfaces. *Opt. Laser Eng.* **2019**, *116*, 68–74. [[CrossRef](#)]
57. Qiu, M.F.; Delic, A.; Raeymaekers, B. The Effect of Texture Shape on the Load-Carrying Capacity of Gas-Lubricated Parallel Slider Bearings. *Tribol. Lett.* **2012**, *48*, 315–327. [[CrossRef](#)]
58. Zhang, Y.L.; Zhang, X.G.; Matsoukas, G. Numerical study of surface texturing for improving tribological properties of ultra-high molecular weight polyethylene. *Biosurf. Biotribol.* **2015**, *1*, 270–277. [[CrossRef](#)]
59. Suh, M.S.; Chae, Y.H.; Kim, S.S.; Hinoki, T.; Kohyama, A. Effect of geometrical parameters in micro-grooved crosshatch pattern under lubricated sliding friction. *Tribol. Int.* **2010**, *43*, 1508–1517. [[CrossRef](#)]
60. Hsu, S.M.; Jing, Y.; Zhao, F. Self-adaptive surface texture design for friction reduction across the lubrication regimes. *Surf. Topogr. Metrol. Prop.* **2016**, *4*, 014004. [[CrossRef](#)]
61. Ding, S.P.; Xu, J.; Liu, P.F.; Shi, Z.L.; Yang, O.X.; Hu, Y.P. Geometric influence on friction and wear performance of cast iron with a micro-dimpled surface. *Results Eng.* **2021**, *9*, 100211. [[CrossRef](#)]
62. Yuan, S.H.; Huang, W.; Wang, X.L. Orientation effects of micro-grooves on sliding surfaces. *Tribol. Int.* **2011**, *44*, 1047–1054. [[CrossRef](#)]
63. Galda, L.; Pawlus, P.; Sep, J. Dimples shape and distribution effect on characteristics of Stribeck curve. *Tribol. Int.* **2009**, *42*, 1505–1512. [[CrossRef](#)]
64. Segu, D.Z.; Hwang, P. Friction control by multi-shape textured surface under pin-on-disc test. *Tribol. Int.* **2015**, *91*, 111–117. [[CrossRef](#)]
65. Li, J.B.; Liu, S.; Yu, A.B.; Xiang, S.T. Effect of laser surface texture on CuSn6 bronze sliding against PTFE material under dry friction. *Tribol. Int.* **2018**, *118*, 37–45. [[CrossRef](#)]
66. Zhang, D.Y.; Li, Z.W.; Zhao, F.F.; Gao, F.; Gao, Z.Q.; Zhang, H.; Dong, G.N. Study on tribological behavior of grooved-texture surfaces under sand-oil boundary lubrication conditions. *Tribol. Trans.* **2021**, *64*, 167–177. [[CrossRef](#)]
67. Maldonado-Cortes, D.; Pena-Paras, L.; Martinez, N.R.; Leal, M.P.; Correa, D.I.Q. Tribological characterization of different geometries generated with laser surface texturing for tooling applications. *Wear* **2021**, *477*, 203856. [[CrossRef](#)]
68. Tu, Z.R.; Meng, X.K.; Yi, M.; Peng, X.D. Shape optimization of hydrodynamic textured surfaces for enhancing load-carrying capacity based on level set method. *Tribol. Int.* **2021**, *162*, 107136. [[CrossRef](#)]
69. Meng, F.M.; Yu, H.Y.; Gui, C.; Chen, L. Experimental study of compound texture effect on acoustic performance for lubricated textured surfaces. *Tribol. Int.* **2019**, *133*, 47–54. [[CrossRef](#)]
70. Zhang, H.; Hua, M.; Dong, G.Z.; Zhang, D.Y.; Chen, W.J.; Dong, G.N. Optimization of texture shape based on Genetic Algorithm under unidirectional sliding. *Tribol. Int.* **2017**, *115*, 222–232. [[CrossRef](#)]
71. Wang, W.; He, Y.Y.; Zhao, J.; Mao, J.Y.; Hu, Y.T.; Luo, J.B. Optimization of groove texture profile to improve hydrodynamic lubrication performance: Theory and experiments. *Friction* **2020**, *8*, 83–94. [[CrossRef](#)]
72. Shen, C.; Khonsari, M.M. Effect of Dimple's Internal Structure on Hydrodynamic Lubrication. *Tribol. Lett.* **2013**, *52*, 415–430. [[CrossRef](#)]
73. YNiu, X.; Pang, X.J.; Yue, S.W.; Shangguan, B.; Zhang, Y.Z. The friction and wear behavior of laser textured surfaces in non-conformal contact under starved lubrication. *Wear* **2021**, *476*, 203723. [[CrossRef](#)]
74. Kasem, H.; Stav, O.; Grutmacher, P.; Gachot, C. Effect of Low Depth Surface Texturing on Friction Reduction in Lubricated Sliding Contact. *Lubricants* **2018**, *6*, 62. [[CrossRef](#)]
75. Segu, D.Z.; Lu, C.X.; Hwang, P.; Kang, S.W. Optimization of Tribological Characteristics of a Combined Pattern Textured Surface Using Taguchi Design. *J. Mater. Eng. Perform.* **2021**, *30*, 3786–3794. [[CrossRef](#)]
76. Konig, F.; Rosenkranz, A.; Grutmacher, P.G.; Mucklich, F.; Jacobs, G. Effect of single- and multi-scale surface patterns on the frictional performance of journal bearings A numerical study. *Tribol. Int.* **2020**, *143*, 106041. [[CrossRef](#)]

77. Zhao, H.X.; Sun, Q.Q.; Deng, X.; Cui, J.X. Earthworm-Inspired Rough Polymer Coatings with Self-Replenishing Lubrication for Adaptive Friction-Reduction and Antifouling Surfaces. *Adv. Mater.* **2018**, *30*, 1802141. [[CrossRef](#)]
78. Wang, W.; Zhao, W.H.; Liu, Y.; Zhang, H.; Hua, M.; Dong, G.N.; Tam, H.Y.; Chin, K.S. A Pocket-Textured Surface for Improving the Tribological Properties of Point Contact under Starved Lubrication. *Materials* **2021**, *14*, 1789. [[CrossRef](#)]
79. Zhang, H.; Liu, Y.; Hafezi, M.; Hua, M.; Dong, G.N. A distribution design for circular concave textures on sectorial thrust bearing pads. *Tribol. Int.* **2020**, *149*, 105733. [[CrossRef](#)]
80. Wang, Q.W.; Yang, Y.; Yao, P.; Zhang, Z.Y.; Yu, S.M.; Zhu, H.T.; Huang, C.Z. Friction and cutting characteristics of micro-textured diamond tools fabricated with femtosecond laser. *Tribol. Int.* **2021**, *154*, 106720. [[CrossRef](#)]
81. Li, X.; Li, Y.H.; Tong, Z.; Ma, Q.; Ni, Y.Q.; Dong, G.N. Enhanced lubrication effect of gallium-based liquid metal with laser textured surface. *Tribol. Int.* **2019**, *129*, 407–415. [[CrossRef](#)]
82. Schneider, J.; Braun, D.; Greiner, C. Laser Textured Surfaces for Mixed Lubrication: Influence of Aspect Ratio, Textured Area and Dimple Arrangement. *Lubricants* **2017**, *5*, 32. [[CrossRef](#)]
83. Hua, M.; Dong, G.N.; Zhang, H.; Ho, J.K.L.; Chow, F.C. The wet tribological behaviors of doughnut patterns laser-textured on DF2 tool steel under different loading conditions. *Appl. Phys. A-Mater.* **2013**, *111*, 997–1011. [[CrossRef](#)]
84. Ren, N.; Nanbu, T.; Yasuda, Y.; Zhu, D.; Wang, Q. Micro textures in concentrated-conformal-contact lubrication: Effect of distribution patterns. *Tribol. Lett.* **2007**, *28*, 275–285. [[CrossRef](#)]
85. Mahdieh, M.H.; Jafarabadi, M.A. Bubble formation induced by nanosecond laser ablation in water and its diagnosis by optical transmission technique. *Appl. Phys. A-Mater.* **2014**, *116*, 1211–1220. [[CrossRef](#)]
86. Nichols, W.T.; Sasaki, T.; Koshizaki, N. Laser ablation of a platinum target in water. III. Laser-induced reactions. *J. Appl. Phys.* **2006**, *100*, 114911. [[CrossRef](#)]
87. Krstulovic, N.; Shannon, S.; Stefanuik, R.; Fanara, C. Underwater-laser drilling of aluminum. *Int. J. Adv. Manuf. Technol.* **2013**, *69*, 1765–1773. [[CrossRef](#)]
88. Zhang, H.; Liu, Y.; Li, B.T.; Hua, M.; Dong, G.N. Improving processing quality and tribological behavior of laser surface textures using oil layer method. *Tribol. Int.* **2020**, *150*, 106353. [[CrossRef](#)]
89. Dai, F.Z.; Wen, D.P.; Zhang, Y.K.; Lu, J.Z.; Ren, X.D.; Zhou, J.Z. Micro-dimple array fabricated on surface of Ti6Al4V with a masked laser ablation method in air and water. *Mater. Des.* **2015**, *84*, 178–184. [[CrossRef](#)]
90. Arjun, K.K.; Anoop, K.K.; Philip, R. Nanosecond laser surface texturing of crystalline silicon in ambient air and water. *AIP Conf. Proc.* **2020**, *2244*, 070010. [[CrossRef](#)]
91. Ren, J.; Kelly, M.; Hesselink, L. Laser ablation of silicon in water with nanosecond and femtosecond pulses. *Opt. Lett.* **2005**, *30*, 1740–1742. [[CrossRef](#)]
92. Zhang, X.Z.; Chen, C.G.; Chen, F.; Zhan, Z.L.; Xie, S.S.; Ye, Q. In vitro investigation on Ho: YAG laser-assisted bone ablation underwater. *Laser Med. Sci.* **2016**, *31*, 891–898. [[CrossRef](#)] [[PubMed](#)]
93. Tsai, C.H.; Li, C.C. Investigation of underwater laser drilling for brittle substrates. *J. Mater. Process. Technol.* **2009**, *209*, 2838–2846. [[CrossRef](#)]
94. Hu, J.; Xu, H.B. Friction and wear behavior analysis of the stainless steel surface fabricated by laser texturing underwater. *Tribol. Int.* **2016**, *102*, 371–377. [[CrossRef](#)]
95. Shulyatyev, V.; Malikov, A.; Orishich, A. The effect of assist gases on the quality of edge surfaces of Al-Li alloys cut with a pulsed Q-switched CO₂ laser. *Optik* **2021**, *231*, 166420. [[CrossRef](#)]
96. Kang, H.W.; Lee, H.; Welch, A.J. Laser ablation in a liquid-confined environment using a nanosecond laser pulse. *J. Appl. Phys.* **2008**, *103*, 083101. [[CrossRef](#)]
97. Wee, L.M.; Ng, E.Y.K.; Prathama, A.H.; Zheng, H. Micro-machining of silicon wafer in air and under water. *Opt. Laser Technol.* **2011**, *43*, 62–71. [[CrossRef](#)]
98. Feng, W.H.; Guo, J.; Yan, W.J.; Wan, Y.C.; Zheng, H.Y. Deep channel fabrication on copper by multi-scan underwater laser machining. *Opt. Laser Technol.* **2019**, *111*, 653–663. [[CrossRef](#)]
99. Xiang, D.H.; Zhang, Z.Q.; Chen, Y.B.; Hu, Y.W.; Lei, X.F. Study of Tribological Properties of Textured Boron-Doped Diamond Film under Water Lubrication. *Surf Interfaces* **2021**, *23*, 100983. [[CrossRef](#)]
100. Zheng, Q.Z.; Fan, Z.J.; Jiang, G.D.; Pan, A.F.; Yan, Z.X.; Lin, Q.Y.; Cui, J.L.; Wang, W.J.; Mei, X.S. Mechanism and morphology control of underwater femtosecond laser microgrooving of silicon carbide ceramics. *Opt. Express* **2019**, *27*, 26264–26280. [[CrossRef](#)]
101. Muhammad, N.; Li, L. Underwater femtosecond laser micromachining of thin nitinol tubes for medical coronary stent manufacture. *Appl. Phys. A-Mater.* **2012**, *107*, 849–861. [[CrossRef](#)]
102. Shaheen, M.E.; Gagnon, J.E.; Fryer, B.J. Femtosecond laser ablation of brass in air and liquid media. *J. Appl. Phys.* **2013**, *113*, 213106. [[CrossRef](#)]
103. Wee, L.M.; Khoong, L.E.; Tan, C.W.; Lim, G.C. Solvent-Assisted Laser Drilling of Silicon Carbide. *Int. J. Appl. Ceram. Technol.* **2011**, *8*, 1263–1276. [[CrossRef](#)]
104. Ouyang, P.X.; Li, P.J.; Leksina, E.G.; Michurin, S.V.; He, L.J. Effect of liquid properties on laser ablation of aluminum and titanium alloys. *Appl. Surf. Sci.* **2016**, *360*, 880–888. [[CrossRef](#)]
105. HWang, X.; Xu, Y.; Zheng, H.Y.; Zhou, W.; Ren, N.F.; Ren, X.D.; Li, T. Monitoring and analysis of millisecond laser drilling process and performance with and without longitudinal magnetic assistance and/or assist gas. *J. Manuf. Process.* **2019**, *48*, 297–312. [[CrossRef](#)]

106. Low, D.K.Y.; Li, L.; Corfe, A.G. Effects of assist gas on the physical characteristics of spatter during laser percussion drilling of NIMONIC 263 alloy. *Appl. Surf. Sci.* **2000**, *154*, 689–695. [[CrossRef](#)]
107. Reg, Y.; Leitz, K.H.; Schmidt, M. Influence of Processing Gas on the Ablation Quality at ns-Laser Beam Ablation, Lasers in Manufacturing 2011. In Proceedings of the Sixth International WIT Conference on Lasers in Manufacturing, Munich, Germany, 23–26 May 2011; Pt B; Volume 12, pp. 182–187. [[CrossRef](#)]
108. Riveiro, A.; Quintero, F.; Lusquinos, F.; Comesana, R.; del Val, J.; Pou, J. The Role of the Assist Gas Nature in Laser Cutting of Aluminum Alloys. *Phys. Proc.* **2011**, *12*, 548–554. [[CrossRef](#)]
109. Antoszewski, B.; Kurp, P. Effect of Surface Texture on the Sliding Pair Lubrication Efficiency. *Lubricants* **2022**, *10*, 80. [[CrossRef](#)]
110. Hsu, C.J.; Stratmann, A.; Medina, S.; Jacobs, G.; Mucklich, F.; Gachot, C. Does laser surface texturing really have a negative impact on the fatigue lifetime of mechanical components? *Friction* **2021**, *9*, 1766–1775. [[CrossRef](#)]
111. Joshi, G.S.; Putignano, C.; Gaudioso, C.; Stark, T.; Kiedrowski, T.; Ancona, A.; Carbone, G. Effects of the micro surface texturing in lubricated non-conformal point contacts. *Tribol. Int.* **2018**, *127*, 296–301. [[CrossRef](#)]
112. Holey, H.; Codrignani, A.; Gumbsch, P.; Pastewka, L. Height-Averaged Navier-Stokes Solver for Hydrodynamic Lubrication. *Tribol. Lett.* **2022**, *70*, 36. [[CrossRef](#)]
113. Rosenkranz, A.; Krupp, F.; Reinert, L.; Mucklich, F.; Sauer, B. Tribological performance of laser-patterned chain links Influence of pattern geometry and periodicity. *Wear* **2017**, *370*, 51–58. [[CrossRef](#)]
114. Aziz, R.; Haq, M.I.U.; Raina, A. Effect of surface texturing on friction behaviour of 3D printed polylactic acid (PLA). *Polym. Test.* **2020**, *85*, 106434. [[CrossRef](#)]
115. Vladescu, S.C.; Ciniero, A.; Tufail, K.; Gangopadhyay, A.; Reddyhoff, T. Optimization of Pocket Geometry for Friction Reduction in Piston-Liner Contacts. *Tribol. Trans.* **2018**, *61*, 522–531. [[CrossRef](#)]
116. FMeng, M.; Zhou, R.; Davis, T.; Cao, J.; Wang, Q.J.; Hua, D.; Liu, J. Study on effect of dimples on friction of parallel surfaces under different sliding conditions. *Appl. Surf. Sci.* **2010**, *256*, 2863–2875. [[CrossRef](#)]
117. Guo, J.; Cheng, J.; Tan, H.; Zhu, S.Y.; Qiao, Z.H.; Yang, J.; Liu, W.M. Ga-based liquid metal: Lubrication and corrosion behaviors at a wide temperature range. *Materialia* **2018**, *4*, 10–19. [[CrossRef](#)]
118. Cheng, J.; Zhu, S.Y.; Tan, H.; Yu, Y.; Yang, J.; Li, W.M. Lead-bismuth liquid metal: Lubrication behaviors. *Wear* **2019**, *430*, 67–72. [[CrossRef](#)]
119. Li, X.; Qi, P.H.; Liu, Q.; Dong, G.N. Improving tribological behaviors of gallium-based liquid metal by h-BN nano-additive. *Wear* **2021**, *484*, 203852. [[CrossRef](#)]
120. Dai, W.; Kheireddin, B.; Gao, H.; Liang, H. Roles of nanoparticles in oil lubrication. *Tribol. Int.* **2016**, *102*, 88–98. [[CrossRef](#)]
121. Gulzar, M.; Masjuki, H.H.; Kalam, M.A.; Varman, M.; Zulkifli, N.W.M.; Mufti, R.A.; Zahid, R. Tribological performance of nanoparticles as lubricating oil additives. *J. Nanopart. Res.* **2016**, *18*, 223. [[CrossRef](#)]
122. Guglea, D.; Ionescu, T.F.; Dima, D.; Georgescu, C.; Deleanu, L. Tribological behavior of rapeseed oil additivated with boron nitride. *IOP Conf. Ser.-Mater. Sci.* **2020**, *724*, 012046. [[CrossRef](#)]
123. Kumari, S.; Sharma, O.P.; Khatri, O.P. Alkylamine-functionalized hexagonal boron nitride nanoplatelets as a novel material for the reduction of friction and wear. *Phys. Chem. Chem. Phys.* **2016**, *18*, 22879–22888. [[CrossRef](#)] [[PubMed](#)]
124. Zhang, J.; Lu, G.C.; Shi, X.L.; Yang, Z.Y.; Xue, Y.W.; Zhou, H.Y. Improving Tribological Performance of Inconel 625 by Combining Groove-Textured Surfaces with Sn-Ag-Cu Solid Lubricant. *J. Mater. Eng. Perform.* **2021**, *30*, 154–164. [[CrossRef](#)]
125. Fu, J.G.; Xu, C.Q.; Ma, D.Q.; Zhu, X.H.; Cheng, D.; Yan, Z.J.; Ma, C.S.; Liu, G.S.; Fu, Y.Y. Tribological properties and releasing behavior of solid lubricant WS₂ in the dimples on cylinder liner surface of diesel engine. *Tribol. Int.* **2021**, *158*, 106936. [[CrossRef](#)]
126. Koszela, W.; Pawlus, P.; Reizer, R.; Liskiewicz, T. The combined effect of surface texturing and DLC coating on the functional properties of internal combustion engines. *Tribol. Int.* **2018**, *127*, 470–477. [[CrossRef](#)]
127. Meng, R.; Deng, J.X.; Duan, R.; Liu, Y.Y.; Zhang, G.L. Modifying tribological performances of AISI 316 stainless steel surfaces by laser surface texturing and various solid lubricants. *Opt. Laser Technol.* **2019**, *109*, 401–411. [[CrossRef](#)]
128. Arenas, M.A.; Ahuir-Torres, J.I.; Garcia, I.; Carvajal, H.; de Damborenea, J. Tribological behaviour of laser textured Ti6Al4V alloy coated with MoS₂ and graphene. *Tribol. Int.* **2018**, *128*, 240–247. [[CrossRef](#)]
129. Zhang, Z.; Yamaguchi, E.S.; Kasrai, M.; Bancroft, G.M. Tribofilms generated from ZDDP and DDP on steel surfaces: Part 1, growth, wear and morphology. *Tribol. Lett.* **2005**, *19*, 211–220. [[CrossRef](#)]
130. Hsu, C.J.; Stratmann, A.; Rosenkranz, A.; Gachot, C. Enhanced Growth of ZDDP-Based Tribofilms on Laser-Interference Patterned Cylinder Roller Bearings. *Lubricants* **2017**, *5*, 39. [[CrossRef](#)]
131. Segu, D.Z.; Kim, J.H.; Choi, S.G.; Jung, Y.S.; Kim, S.S. Application of Taguchi techniques to study friction and wear properties of MoS₂ coatings deposited on laser textured surface. *Surf. Coat. Technol.* **2013**, *232*, 504–514. [[CrossRef](#)]
132. XWang, L.; Adachi, K.; Otsuka, K.; Kato, K. Optimization of the surface texture for silicon carbide sliding in water. *Appl. Surf. Sci.* **2006**, *253*, 1282–1286. [[CrossRef](#)]
133. Wang, Z.Q.; Fu, Q.; Wood, R.J.K.; Wu, J.; Wang, S.C. Influence of bionic non-smooth surface texture on tribological characteristics of carbon-fiber-reinforced polyetheretherketone under seawater lubrication. *Tribol. Int.* **2020**, *144*, 106100. [[CrossRef](#)]
134. Li, X.; Wang, Z.K.; Dong, G.N. Preparation of nanoscale liquid metal droplet wrapped with chitosan and its tribological properties as water-based lubricant additive. *Tribol. Int.* **2020**, *148*, 106349. [[CrossRef](#)]
135. Bai, P.P.; Li, S.W.; Jia, W.P.; Ma, L.R.; Meng, Y.G.; Tian, Y. Environmental atmosphere effect on lubrication performance of gallium-based liquid metal. *Tribol. Int.* **2020**, *141*, 105904. [[CrossRef](#)]

136. Qi, P.H.; Wang, S.J.; Li, J.; Li, Y.; Dong, G.N. Synergistic lubrication effect of antioxidant and low content ZDDP on PFPE grease. *Ind. Lubr. Tribol.* **2021**, *73*, 830–838. [[CrossRef](#)]
137. Li, X.; Yan, C.; Liu, Q.; Dong, G.N. An In Situ Fabrication of CuGa₂ Film on Copper Surface With Improved Tribological Properties. *J. Tribol.* **2021**, *143*, 071404. [[CrossRef](#)]
138. Li, X.; Lu, H.L.; Guo, J.D.; Tong, Z.; Dong, G.N. Synergistic water lubrication effect of self-assembled nanofilm and graphene oxide additive. *Appl. Surf. Sci.* **2018**, *455*, 1070–1077. [[CrossRef](#)]
139. Li, X.; Liu, Q.; Dong, G.N. Self-assembly membrane on textured surface for enhancing lubricity of graphene oxide nano-additive. *Appl. Surf. Sci.* **2020**, *505*, 144572. [[CrossRef](#)]
140. Dalhat, M.A. Water resistance and characteristics of asphalt surfaces treated with micronized-recycled-polypropylene waste: Super-hydrophobicity. *Constr. Build. Mater.* **2021**, *285*, 122870. [[CrossRef](#)]
141. Dongre, G.; Rajurkar, A.; Raut, R.; Jangam, S. Preparation of super-hydrophobic textures by using nanosecond pulsed laser. *Mater. Today Proc.* **2021**, *42*, 1145–1151. [[CrossRef](#)]
142. Emelyanenko, A.M.; Shagieva, F.M.; Domantovsky, A.G.; Boinovich, L.B. Nanosecond laser micro- and nanotexturing for the design of a superhydrophobic coating robust against long-term contact with water, cavitation, and abrasion. *Appl. Surf. Sci.* **2015**, *332*, 513–517. [[CrossRef](#)]
143. Ta, V.D.; Dunn, A.; Wasley, T.J.; Li, J.; Kay, R.W.; Stringer, J.; Smith, P.J.; Esenturk, E.; Connaughton, C.; Shephard, J.D. Laser textured superhydrophobic surfaces and their applications for homogeneous spot deposition. *Appl. Surf. Sci.* **2016**, *365*, 153–159. [[CrossRef](#)]
144. Hong, S.H.; Kim, M.H.; Yun, H.W.; Paik, T.; Lee, H. Solution-processed fabrication of superhydrophobic hierarchical zinc oxide nanostructures via nanotransfer printing and hydrothermal growth. *Surf. Coat. Technol.* **2017**, *331*, 189–195. [[CrossRef](#)]
145. Boinovich, L.B.; Modin, E.B.; Sayfutdinova, A.R.; Emelyanenko, K.A.; Vasiliev, A.L.; Emelyanenko, A.M. Combination of Functional Nanoengineering and Nanosecond Laser Texturing for Design of Superhydrophobic Aluminum Alloy with Exceptional Mechanical and Chemical Properties. *ACS Nano* **2017**, *11*, 10113–10123. [[CrossRef](#)] [[PubMed](#)]
146. Feng, X.M.; Sun, P.F.; Tian, G.Z. Recent Developments of Superhydrophobic Surfaces (SHS) for Underwater Drag Reduction Opportunities and Challenges. *Adv. Mater. Interfaces* **2022**, *9*, 2101616. [[CrossRef](#)]
147. HDong, Y.; Cheng, M.J.; Zhang, Y.J.; Wei, H.; Shi, F. Extraordinary drag-reducing effect of a superhydrophobic coating on a macroscopic model ship at high speed. *J. Mater. Chem. A* **2013**, *1*, 5886–5891. [[CrossRef](#)]
148. Ibrahim, M.D.; Amran, S.N.A.; Yunus, Y.S.; Rahman, M.R.A.; Mohtar, M.Z.; Wong, L.K.; Zulkharnain, A. The Study of Drag Reduction on Ships Inspired by Simplified Shark Skin Imitation. *Appl. Bionics Biomech.* **2018**, *2018*, 7854321. [[CrossRef](#)]
149. Yu, C.M.; Liu, M.F.; Zhang, C.H.; Yan, H.; Zhang, M.H.; Wu, Q.S.; Liu, M.J.; Jiang, L. Bio-inspired drag reduction: From nature organisms to artificial functional. *Giant* **2020**, *2*, 100017. [[CrossRef](#)]
150. Qin, L.G.; Ma, Z.Y.; Sun, H.J.; Lu, S.; Zeng, Q.F.; Zhang, Y.L.; Dong, G.N. Drag reduction and antifouling properties of non-smooth surfaces modified with ZIF-67. *Surf. Coat. Technol.* **2021**, *427*, 127836. [[CrossRef](#)]
151. Wu, L.; Qin, W.; He, Y.Z.; Zhu, W.F.; Ren, X.H.; York, P.; Xiao, T.Q.; Yin, X.Z.; Zhang, J.W. Material distributions and functional structures in probiotic microcapsules. *Eur. J. Pharm. Sci.* **2018**, *122*, 1–8. [[CrossRef](#)]
152. Dai, W.; Alkahtani, M.; Hemmer, P.R.; Liang, H. Drag-reduction of 3D printed shark-skin-like surfaces. *Friction* **2019**, *7*, 603–612. [[CrossRef](#)]
153. Emami, B.; Hemeda, A.A.; Amrei, M.M.; Luzar, A.; Gad-el-Hak, M.; Tafreshi, H.V. Predicting longevity of submerged superhydrophobic surfaces with parallel grooves. *Phys. Fluids* **2013**, *25*, 062108. [[CrossRef](#)]
154. Xue, Y.W.; Shi, X.L.; Zhou, H.Y.; Yang, Z.Y.; Zhang, J.; Wu, C.H.; Xue, B. Effects of Textured Surface Combined with Sn-Ag-Cu Coating on Tribological Properties and Friction-Induced Noise of Ti-6Al-4V Alloy. *Tribol. Trans.* **2021**, *64*, 562–577. [[CrossRef](#)]
155. Xue, Y.W.; Shi, X.L.; Zhou, H.Y.; Lu, G.C.; Zhang, J. Effects of groove-textured surface combined with Sn-Ag-Cu lubricant on friction-induced vibration and noise of GCr15 bearing steel. *Tribol. Int.* **2020**, *148*, 106316. [[CrossRef](#)]
156. Mo, J.L.; Wang, Z.G.; Chen, G.X.; Shao, T.M.; Zhu, M.H.; Zhou, Z.R. The effect of groove-textured surface on friction and wear and friction-induced vibration and noise. *Wear* **2013**, *301*, 671–681. [[CrossRef](#)]
157. Yang, J.; Liu, Z.L.; Cheng, Q.C.; Liu, X.K.; Deng, T.Y. The effect of wear on the frictional vibration suppression of water-lubricated rubber slat with/without surface texture. *Wear* **2019**, *426*, 1304–1317. [[CrossRef](#)]
158. Liu, X.Y.; Shi, X.L.; Huang, Y.C.; Deng, X.B.; Lu, G.C.; Yan, Z.; Xue, B. Tribological behavior and self-healing functionality of M50 material covered with surface micropores filled with Sn-Ag-Cu. *Tribol. Int.* **2018**, *128*, 365–375. [[CrossRef](#)]